

## **Perspective and Potential of Smart Optical Materials**

**Sang H. Choi**

NASA Langley Research Center, Hampton, VA 23681, USA

**Adam J. Duzik and Hyun-Jung Kim**

National Institute of Aerospace, Hampton, VA 23666, USA

**Yeonjoon Park**

Dronicar Inc., Yorktown, VA 23693, USA

**Jaehwan Kim, Hyun-U Ko, and Hyun-Chan Kim**

Creative Research Center for Nanocellulose Future Composites, Inha University, Nam-ku, Incheon 22212, South Korea

**Sungryul Yun, and Ki-Uk Kyung**

Electronics and Telecommunications Research Institute (ETRI), Yuseong-gu, Daejeon 34129, South Korea

### **Abstract:**

The increasing requirements of hyperspectral imaging optics, electro/photo-chromic materials, negative refractive index metamaterial optics, and miniaturized optical components from micro-scale to quantum-scale optics have all contributed to new features and advancements in optics technology. Development of multifunctional capable optics has pushed the boundaries of optics into new fields that require new disciplines and materials to maximize the potential benefits. The purpose of this study is to understand and show the fundamental materials and fabrication technology for field-controlled spectrally active optics (referred to as smart optics) that are essential for future industrial, scientific, military, and space applications, such as membrane optics, light detection and ranging (LIDAR) filters, windows for sensors and probes, telescopes, spectrometers, cameras, light valves, light switches, and flat-panel displays. The proposed smart optics are based on the Stark and Zeeman effects in materials tailored with quantum dot arrays and thin films made from readily polarizable materials via ferroelectricity or ferromagnetism. Bound excitonic states of organic crystals are also capable of optical adaptability, tunability, and reconfigurability. To show the benefits of smart optics, this paper reviews spectral characteristics of smart optical materials and device technology. Experiments testing the quantum-confined Stark effect, arising from rare earth element doping effects in semiconductors, and applied electric field effects on spectral and refractive index are discussed. Other bulk and dopant materials were also discovered to have the same aspect of shifts in spectrum and refractive index. Other efforts focus on materials for creating field-controlled spectrally smart active optics (FCSAO) on a selected spectral range. Surface plasmon polariton transmission of light through apertures is also discussed, along with potential applications. New breakthroughs in micro scale multiple zone plate optics as a micro convex lens are reviewed, along with the newly discovered pseudo-focal point not predicted with conventional optics modeling. Micron-sized solid state beam scanner chips for laser waveguides are reviewed as well.

**Keywords:** Smart Optics, Smart Optical Materials, Quantum Optics, Metamaterials

## **I. Introduction**

Conventional optics use wide bandgap materials for spectral stability and to prevent optical deviation and aberration. On the other hand, a newly emerging concept, smart optical devices, utilizes optical deviation and aberration in narrow bandgap optical materials. Modern LIDAR technology is an example. The selective measurement capability of spectral lines captured by LIDAR's primary reflector permits high resolution of the spectral signature of an unidentified emitter. Such smart optical devices require certain optical properties to be instantaneously and flexibly controllable in response to programmed measurement scenarios not found in conventional optics. In these devices, applied electric and magnetic fields, and thermal gradients, alter properties such as propagation, reflection, refractive index, absorption, and transmission, either separately or together. Precise tunability of optical properties offers new applications impossible with conventional optics.

These smart optical materials (SOM) change properties based on one of the following properties or effects: Electro- or magneto-absorption changes,[1,2] the Franz-Keldysh effect,[3] the quantum-confined Stark effect,[4] the Zeeman effect,[5] the electrochromic effect,[6] the Pockels effect,[7] the Kerr effect,[8] electro or magneto gyration,[9,10] the electron-refractive effect.[11,12] When an electromagnetic (EM) wave propagates through a medium that has a property of smart optical materials, the wave nature can be altered by an applied field. Such a change may appear as spectral shift of the incident EM wave and/or as a shift in refractive index.

### **I-1. Concept of Smart Optics and Quantum Optics**

Field-controlled spectrally smart active optics (FCSAO) are reconfigurable devices based on thin-film or quantum dot structures. In an external applied field, quantum electronic (weaker effect) and dipole moment (stronger effect) behavior can be adapted to applications such as changeable spectral filters. Conventional optical filters are fundamentally limited to a broadly or narrowly fixed band-pass filtering or flux intensity. For line spectrum or narrow bandwidth filters, conventional optics require gratings to resolve the spectral band. The Fabry-Perot narrow bandwidth filter is a multilayer device that filters via a cavity of particular thickness bounded by two partial reflectors.[13] However, this concept is spectrally fixed, limiting its applicability to a narrow range of conditions. Applications requiring high resolution at a wide range of wavelengths necessitates multiple devices.

#### **I-1-1. Quantum Electronic Constraint – Stark Effects**

The Stark effect occurs when externally applied fields lift the degeneracy of the angular momentum states.[14] As a quantum effect, the response time is low compared to other optical effects. Thus, the Stark effect is a potentially effective means for selective spectral filtering. A quantum confined Stark effect (QCSE) optical modulator element has one or more quantum wells each bounded by asymmetric barriers. When an electric field is applied, the absorption edge shifts proportionally to the field intensity. The goal is to use the Stark effect to produce either the shift in refractive indices or shift in spectral responses of materials. As compared to the intrinsic Stark effect due to the quantum transitions of bound or transitional electrons, the QCSE causes a charge redistribution within wide bandgap materials according to the applied electric field. This changes the absorption of incoming photons. According to the Kramers-Kronig

relations (KKR) for linear and non-linear optics,[15,16] the refractive index profile and the chromatic dispersion are functions of frequency-dependent losses

$$n(\omega) = 1 + \frac{c}{\pi} \wp \int_0^{\infty} \frac{\alpha(\omega^*)}{\omega^{*2} - \omega^2} d\omega^* \quad (1)$$

Where  $\alpha(\omega)$  is intensity absorption coefficient,  $\omega$  is the frequency ( $\omega^*$  is a dummy variable of integration), and  $\wp$  denotes the Cauchy principle value, which requires some manipulation when such an integral is numerically calculated. The index of refraction is determined by the change in the absorption coefficient in the media. Therefore, the applied electric field indirectly affects the index of refraction. In a wide band-gap semiconductor, shallow dopant levels give mobile carriers to the conduction band or valence band, while defect-induced deep levels can capture or emit the mobile charges. Figure 1 shows the electro-refractive effect from the ionization of deep levels in the Space-Charge-Region (SCR) made by an applied electric field. Deep levels have large bounding energies inside the bandgap of the semiconductor. Without the electric field, the deepest levels are in the neutral state. After the electric field is applied, the charges redistribute in the SCR. Therefore, the deep levels in the anode side are positively charged and the deep levels in the cathode side are negatively charged, while the ionization of deep levels produces new unoccupied states for optical transitions. The change of refractive index is controlled by the density and location of deep levels in this model. Additional Deep Level Transition Spectroscopy (DLTS) measurements can identify these embedded deep levels.[17] The top of Figure 1 shows the deep and shallow dopant levels in a wide bandgap material. Without the applied electric field, mobile electrons are distributed uniformly in the media layer. Most of the deep levels are neutral in this state. Parts (1) and (2) of Figure 1 show the effects of the electric field on charge distribution. With a strong applied electric field, the electrons are re-distributed and the deep levels are ionized and form new color centers, changing the absorption coefficient and the index of refraction. While the Stark effect is effective in changing the absorption and re-emission, this requires several volts to shift the Fermi level. Such a bias voltage requires a rather high amount of power, limiting this effect in applications where power is at a premium.

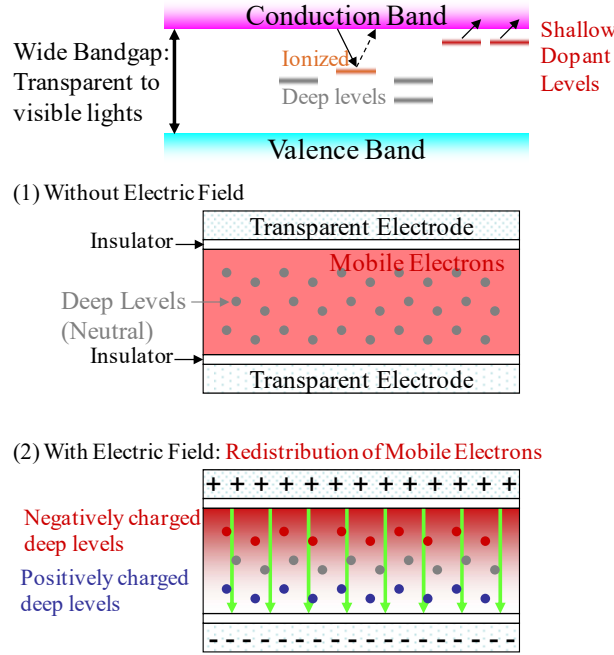


**Figure 1. Description of Kramers-Kronig Relations for the re-distributed charges by an applied electric field.**

### I-1-2. Quantum Electronic Constraint – Zeeman Effects

An external applied magnetic field produces the Zeeman effect, a level splitting of the coupled angular momenta.[5,14] The total Hamiltonian ( $H$ ) of an atom in an applied magnetic field that has two components is:

$$H = H_o + V_M \quad (2)$$

where  $H_o$  is the unperturbed Hamiltonian of the atom and  $V_M$  is the perturbation caused by the applied magnetic field. The magnetic potential energy of the atom in the applied field is described by

$$\langle V_M \rangle = \frac{\mu_B}{\hbar} \vec{J} \left( g_L \frac{\vec{L} \cdot \vec{J}}{J^2} + g_S \frac{\vec{S} \cdot \vec{J}}{J^2} \right) \cdot \vec{B} \quad (3)$$

where  $\mu_B$  is the Bohr magnetron,  $\hbar$  the Planck constant, and  $g_L$  and  $g_S$  are the Lande g-factors along with the angular momentum ( $\vec{L}$ ) and spin-orbit momentum ( $\vec{S}$ ), respectively. The orbital angular momentum vector ( $\vec{L}$ ) coupled to the spin-orbit momentum vector ( $\vec{S}$ ), precesses around the total angular momentum vector ( $\vec{J}$ ) when the Zeeman energy is much less than spin-orbit interaction energy. However, as the field strength increases, the angular and spin-orbit momenta individually are decoupled and begin to precess around the field vector ( $\vec{B}$ ). In both cases, the Zeeman effect lifts degeneracy causing level splittings resulting in spectral variations. The Zeeman effect is more vivid for polyatomic molecules due largely to the asymmetrical nature of the molecular structures and complex state levels. As such, the Zeeman effect shifts the radiative transitions, emission, absorption, and transmission spectra, and is stronger and wider ranged than the Stark effect. Hence, the impinging light on Zeeman-affected materials may be selectively gated

for the color (spectrally variable) rather than bleach (flux density control) by modulating the externally applied fields. As with the Stark effect, the Zeeman effect requires a rather high power input, with the added disadvantage of conversion losses in generating the magnetic field. In applications with little space and weight to spare, this is a difficult shortcoming.

### I-1-3. Electrochromism

Electrochromism is based on the ionic state changes that give rise to the colored or bleached state from either anodic or cathodic charge. Figure 2 shows a typical arrangement of electrochromic layers. Electrochromic materials, both organic and inorganic, have widespread applications in light attenuation, displays and analysis. Previous efforts have resulted in a few techniques such as thermo-, photo-, and electro-chromisms (TC, PC, and EC), but never fully realized the potential for actual optical instrument applications.[18] The most notable shortcomings of chromism are slow responsiveness (TC and EC), limited flux density control (TC, PC, and EC) rather than spectral control, and selection-dependence of chromogenics that embrace both organic and inorganic substances. The shortcomings of electrochromism originate from the low ion mobility in the electrolyte. This is due to the ionic state varying with total injected or ejected charges. Moreover, current electrochromic devices suffer from needing a rather large number of layers, complicating manufacturing. Moreover, these often need organic molecules, leading to outgassing problems and possible breakdown in vacuum and other extreme environments.

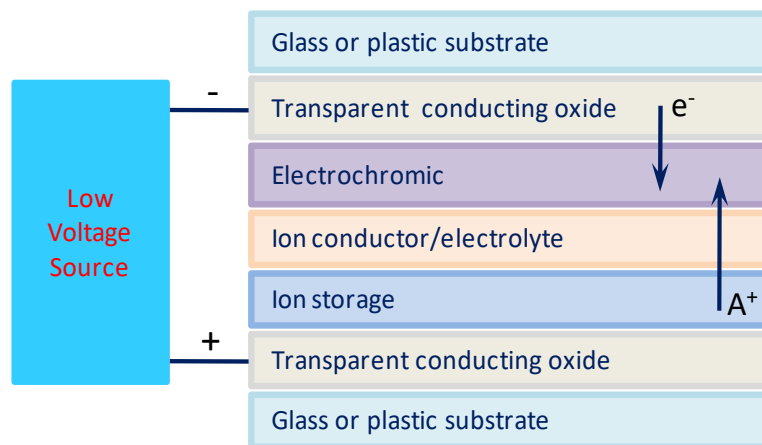


**Figure 2: Electrochromism device concept. [19]**

Figure 3 shows an example for the optical transmission spectra of PolyProDOT-Me<sub>2</sub>-coated Al-nanoslit structures with respective values of slit period P with 240, 270, 300, 330, 360 and 390 nm, along with corresponding optical micrographs of device areas imaged in transmission. As incident light is injected into the nanoslit array, an electrochemical redox reaction takes place in the electrolyte. Ions move within the electrolyte, causing a color change in what light is transmitted that is dependent upon the ion mobility and applied voltage. In order to study optical modulation characteristics, a reflecting coating was not applied on the inner substrate. Optical modulation of the device was then measured in terms of transmittance modulation. In the neutral (unoxidized) OFF-state, the device appears black in color as shown in Figure 3d.[20] Under an applied voltage and injected light, the reduction reaction occurs in the electrolyte, resulting in the ON-state in

Figure 3c. By reversing the polarity of applied voltage, PolyProDOT-Me<sub>2</sub>-coated Al-nanoslit structures are oxidized and appears darkish black colored. In this state, the transmittance is reduced over short wavelengths up to 460nm except for the increase in the wavelength range of approximately 400-700nm, allowing for a strong modulation of the solar spectrum from 400 nm to 700 nm.

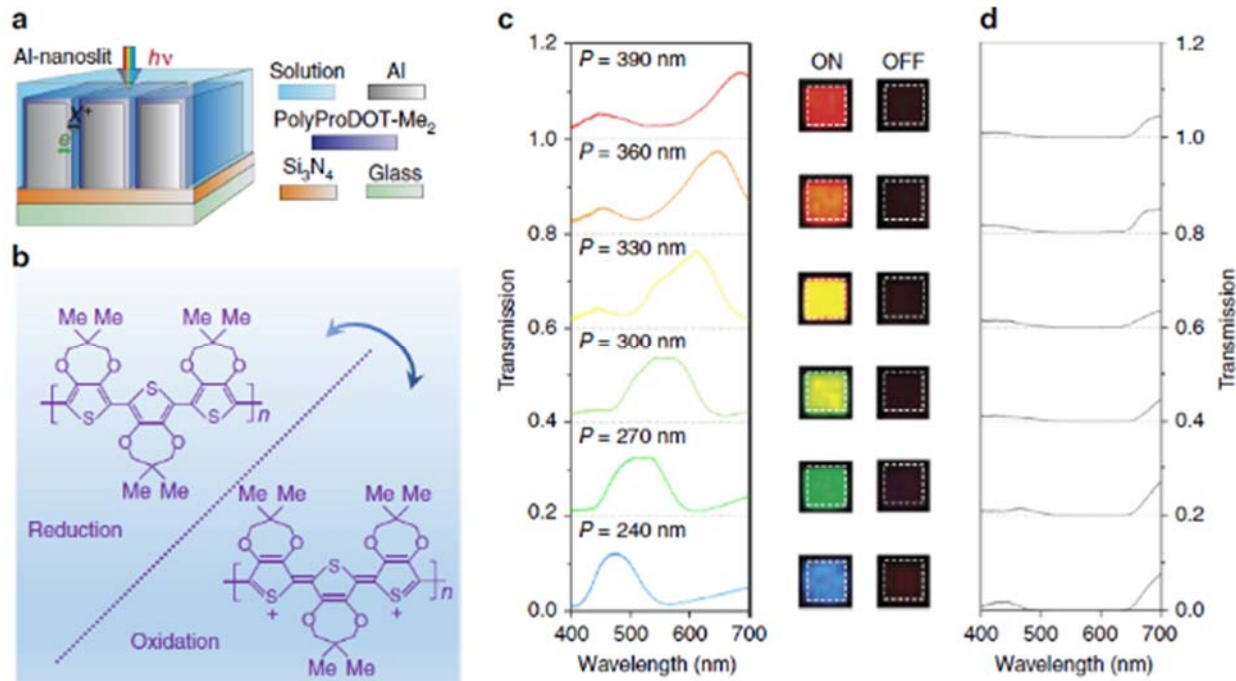


**Figure 3. Transmission spectra of PolyProDOT-Me<sub>2</sub>-coated Al-nanoslit structures. Color variation by applied voltage is clearly shown in (c). [20]**

#### I-1-4. Organic Materials with Quantum Effects

Organic and inorganic II-VI and III-V semiconductors all show excitonic effects on optical and electronic properties.[21] An exciton is a bound electron-and-hole pair that transports energy through a solid. Bound excitons of an ordered organic crystalline structure (i.e. aluminum tris[8-hydroxyquinoline] or Alq<sub>3</sub>) exhibit electroluminescence (EL) and photoluminescence (PL) upon injection of electron-hole pairs.[22] As such, future work will harness organic crystals for FCSAO development.

Figure 4 shows the concept of spectrally active smart optics. A quantum-dot array, a thin-film of Zeeman or Stark material, or a thin-film organic crystal is grown on an optical window substrate for smart active optical filtering. Quantum dot sizes are on the order of tens of nanometers. FCSAO devices possess significant advantages in fast response times due to the quantum Stark and Zeeman effects and in applied field suppression of thermal noise.

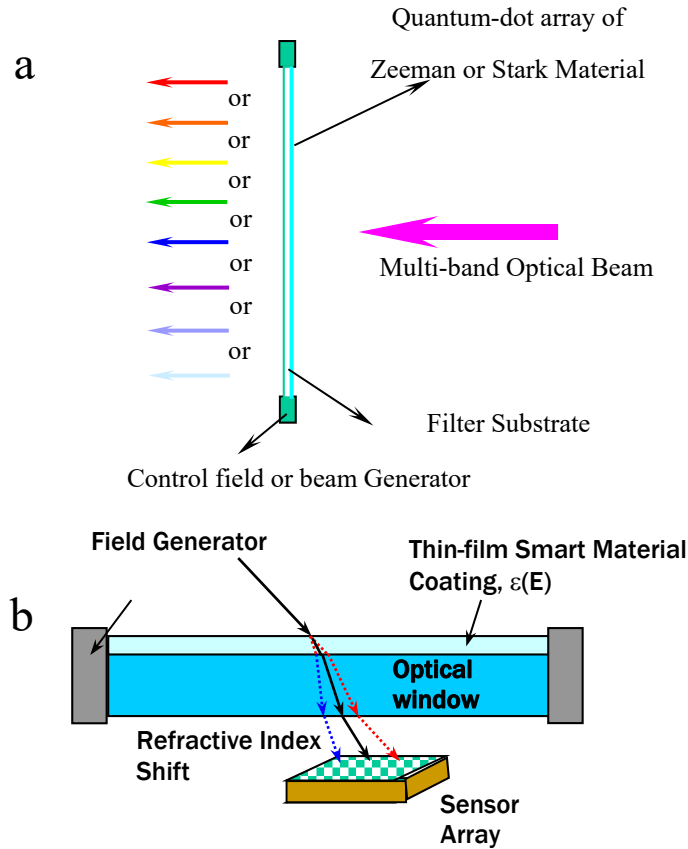


**Figure 4. (a) Zeeman or Stark effects and (b) lattice structure change effects on photoemission.**

## **I-2. Electro-Optics and Magneto-Optics**

The electro-optic (EO) and magneto-optic (MO) materials generally alter optical properties by certain measurable changes in quantum state under the influence of an electric or magnetic field. The interaction between the applied field and the electronic states of materials results in the change in optical properties of domain, such as birefringence under electric field and rotation of polarization under magnetic field. Birefringence is an optically anisotropic phenomena, where the refractive index of a material is determined by the polarization and propagation of light.[23] The maximum difference between refractive indices in the EO material is readily measured and quantified by the split refracted paths between parallel and perpendicular polarizations. In other words, such a phenomenon of birefringence is observed as a double refraction whereby a beam of incident light is split by polarization into two beams passing through with slightly different paths. Non-cubic crystals such as calcite ( $\text{CaCO}_3$  -trigonal), rutile ( $\text{TiO}_2$  -tetragonal), and perovskite ( $\text{CaTiO}_3$  -orthorhombic) show strong birefringent effects. Well-known device applications of electro-optics include the Kerr cell, which uses a liquid whose birefringence has a square power responsivity to an electric field. Another application is the Pockels cell, which uses a crystal with a linear responsivity to an electric field. Some polymeric materials under mechanical stress exhibit the Pockels effect due to the nonlinear optical chromophores in a polymer lattice.[24,25] Other applications of birefringent materials are liquid crystal displays,[26] light modulators,[27] Lyot

filter,[28] second harmonic generators,[29] non-linear optics,[30] medical diagnostics,[31] photoelasticity by stress-induced birefringence,[32] seismology,[33] and mineralogy.[34]

Gyrotropic or gyromagnetic materials are those whose polarization plane rotates with the quasistatic magnetic field. The rotation of polarization plane is regarded as a Faraday rotator, resulting in the Faraday effect when light transmits through the material. This is represented in Eq. (4) as the change in the permittivity tensor of the material by either externally applied magnetic field or ferromagnetic nature of material. When the gyration vector  $\mathbf{g} = \varepsilon_o \chi^{(m)} \mathbf{H}$  (where  $\chi^{(m)}$  is the magneto-optical susceptibility and  $\mathbf{H}$  is the applied magnetic field) lies along the same direction, Eq. (4) can be expressed as:

$$\varepsilon = \begin{pmatrix} \varepsilon_1 & +ig_z & 0 \\ -ig_z & \varepsilon_2 & 0 \\ 0 & 0 & \varepsilon_3 \end{pmatrix} \quad (4)$$

In the above case the solutions are elliptically polarized electromagnetic waves with phase velocities  $1/\sqrt{\mu(\varepsilon_1 \pm g_z)}$  (where  $\mu$  is the magnetic permeability). This difference in phase velocities leads to the Faraday effect. For the case of light propagating purely perpendicular to the gyration vector, the properties are known as the Cotton-Mouton effect and used for a circulator.[35,36]

### I-3. Controllable Physical Optics

Development of controllable physical optics is essential to industry, military and consumer products applications such as camera lenses, endoscopes, projectors, membrane optics, LIDAR filters, windows for sensors or probes, telescopes, spectrometers, light valves, light switches, and flat-panel displays, etc. The tunable lens is one example of controllable physical optics without the use of moving parts, as shown in Figure 5. It can change not only focal distance, but also reflective index, optical angle and optical intensity by tuning or reconfiguring the lens material itself. Such a lens has broad technological potential in miniaturization and new features such as multi-focus and multi-view.



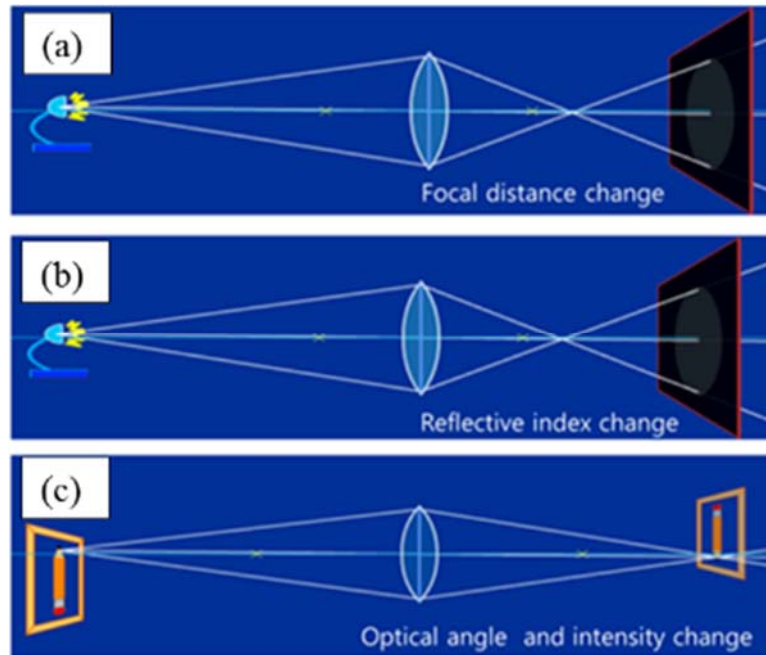


**Figure 5. Tunable lens concept. A lens can change its optical properties through altering (a) its focal length, (b) the refractive index, and (c) the optical angle through shape shifting.**

Since the 1960s, various tunable lenses have been developed, including tunable liquid lenses, tunable polymer lenses and tunable liquid crystal lenses. A tunable lens has to be able to deform its shape or tune its optical properties while maintaining its optical transparency. The liquid lenses use one or more fluids to create variable-focus without any moving parts by controlling curvature or refractive index of liquid. However, the liquid lenses are slow in response and bulky. Tunable polymer lenses use electro-active polymers (EAPs) that deform in the presence of electric field, but also exist in several variations that combine liquid, optical materials and EAPs.

## II. SMART OPTICAL MATERIALS

### II-1. Ferroelectric Materials

Rare-earth (RE) elements have inverted electron-shell structures so that the optical transition can occur in the inner shell instead of the outer shell. As a result, RE elements commonly have very sharp optical lines and long life times, which are less affected by the neighboring atoms. Eu is the most reactive RE element and easily forms Europium Oxide ( $\text{Eu}_2\text{O}_3$ ) which is widely used in phosphor materials with its strong red light ( $\sim 620\text{nm}$ ) emission due to the low threshold impact ionization energy 2.1eV of 5D0 level. Samantaray et al. reported that doping levels as low as 0.1% of Eu in  $\text{BaTiO}_3$  can give a strong red photoluminescence signal at room temperature.[37] Similarly, spectral characteristics of other RE doping elements in  $\text{BaTiO}_3$ , such as samarium (Sm) and dysprosium (Dy) were studied to identify the bands of emission at 563 nm, 596 nm, 643 nm, and 701 nm and excitation spectra at 406 nm.[38] Figure 6 shows a bandgap structure of europium doped  $\text{BaTiO}_3$ . The level transitions in inverted electron-shell of europium appear as clear line emissions with optical sharpness.

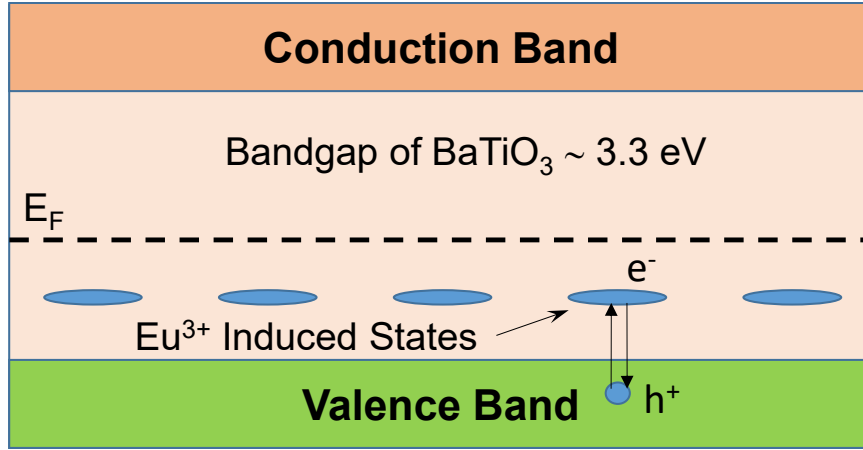


Figure 6. Bandgap model of BaTiO<sub>3</sub> with Eu<sup>3+</sup> dopant.

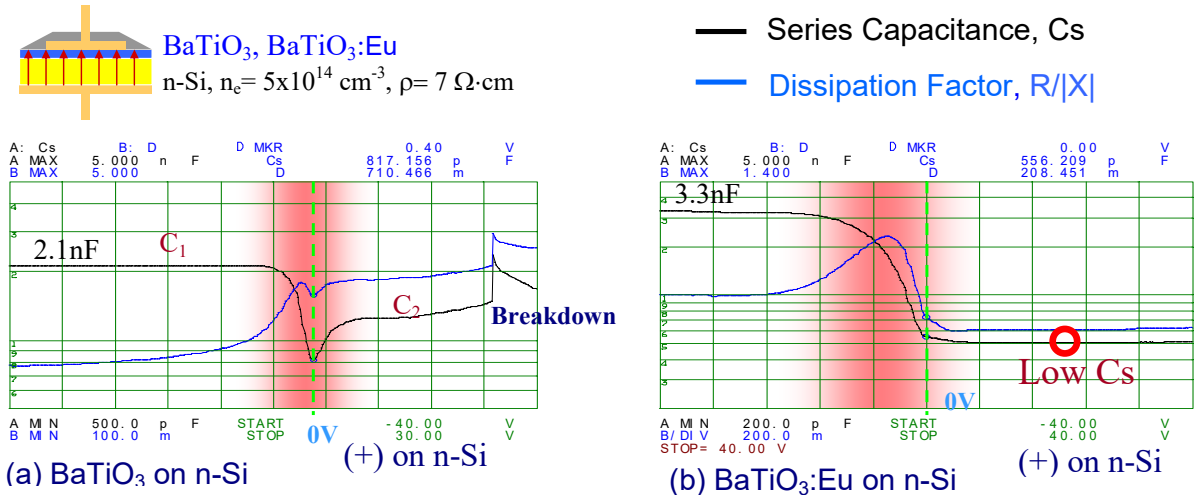


Figure 7. Capacitance-Voltage measurement of (a) BaTiO<sub>3</sub> and (b) BaTiO<sub>3</sub>:Eu.[39]

Figure 7 shows the capacitance-voltage (C-V) data of two different films of BaTiO<sub>3</sub> and BaTiO<sub>3</sub>:Eu. The series capacitance measured in pure BaTiO<sub>3</sub> film in Figure 7(a) has three different regions, which are a constant capacitance  $C_1$ , transition region, another constant capacitance  $C_2$ , and break down. The difference in capacitance  $C_1$  and  $C_2$  are mainly due to the anisotropic stress on the BaTiO<sub>3</sub> film.

The transition zone exists because of the change in the polarization. If the film is homogeneous and isotropic between two identical electrodes, the capacitances  $C_1$  and  $C_2$  have to be the same because they are symmetric. Therefore, the results here show that ITO/BaTiO<sub>3</sub>/n-Si layer structure is close to the ideal ferroelectric capacitor except for the epitaxial stress. On the other hand, the series capacitance measured in the BaTiO<sub>3</sub>:Eu film shows a uniform decrease in the capacitance as the voltage on the n-Si wafer increases. Note the low  $C_s$  in Figure 7(b). A uniform decrease of the capacitance is a typical behavior of the reverse biased diode. In the p-n junction of a diode, the depletion width is controlled by the reverse bias voltage. Since the charge depletion width determines the effective gap-distance of two conductive materials, p-semiconductor and n-semiconductor of a diode that can be viewed as a capacitor in the reverse bias, the capacitance

decreases with the increasing reverse bias voltage. Therefore it can be estimated that Eu incorporation generates more positive charge concentration in BaTiO<sub>3</sub> such that the BaTiO<sub>3</sub>:Eu layer on the n-Si substrate behaves like the p-n junction of a diode.

## II-2. Semimetallic Films

Alloys of amorphous GaN/ScN (Figure 8) and alloys of GaSiN were investigated with a variable angle spectroscopic ellipsometer (VASE). Research was concentrated on Sc<sub>x</sub>Ga<sub>1-x</sub>N systems. These exhibit band-gap engineering, as shown in Figure 9, which could lead to their use as electronic materials, as compared with other work.[40] In particular, these Sc<sub>x</sub>Ga<sub>1-x</sub>N films are promising for producing Fabry-Perot type filters with controllable properties. The index of refraction  $n$  was found to vary with film composition as shown in Figure 10 while the extinction coefficient  $k$  remained almost constant for the same range of wavelength (see Figure 11).

The lattice mismatch between GaN (0001) and ScN (111) is only **0.2%**<sup>[1]</sup>

GaN (Wurtzite):  $a = 3.189 \text{ \AA}$   
 $c = 5.185 \text{ \AA}$

ScN (NaCl):  $a = 4.50 \text{ \AA}$   
in (111):  $a' = 3.182 \text{ \AA}$

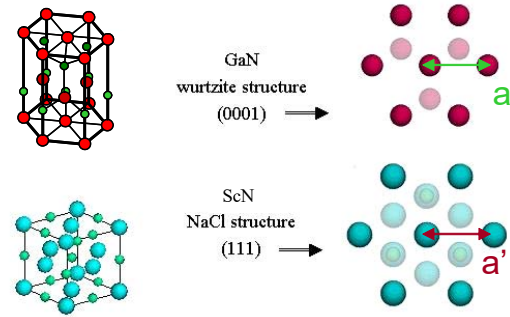


Figure 8. Crystal structure and lattice constant of ScN and GaN.

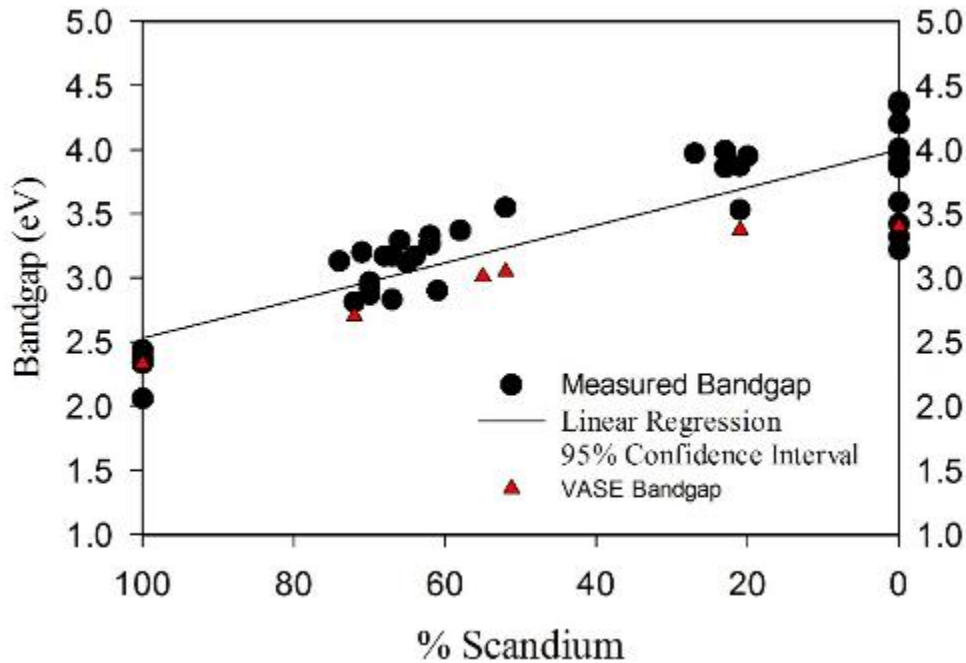
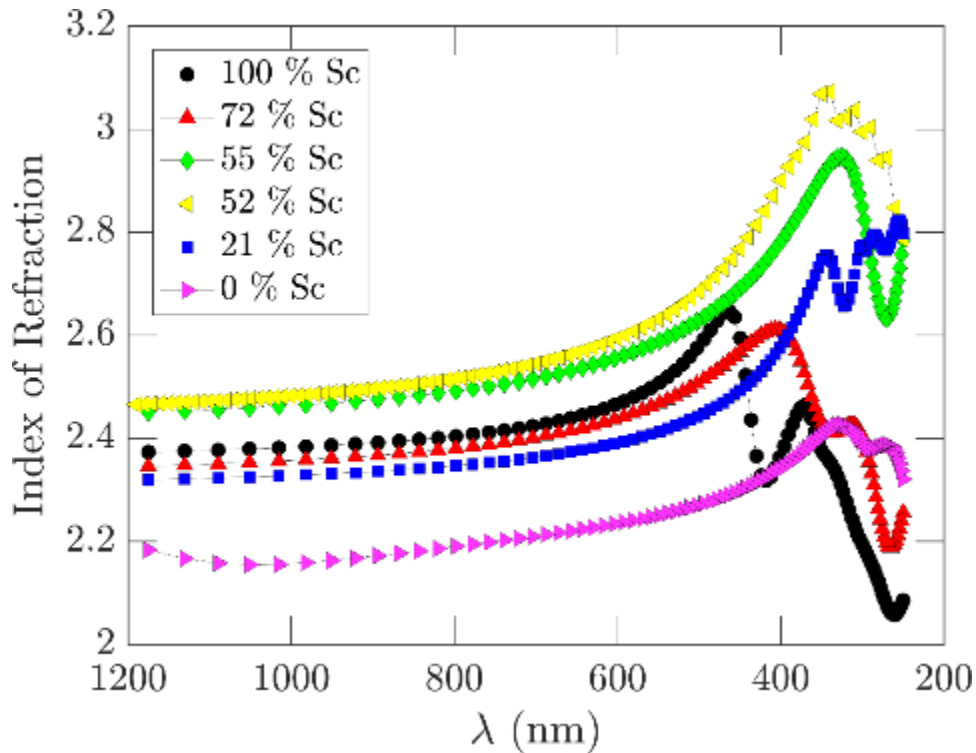


Figure 9. Optical bandgap versus Scandium concentration.[40]

The VASE machine was modified to apply a potential to the films during measurement. For most films no effect was seen. One film of amorphous/microcrystalline ScN, however, shows a slight decrease in index of refraction and extinction coefficient over the range 4-5 eV with increasing applied voltage as shown in Figure 12 and Figure 13. The film was measured with zero, 1000, and 1500 volts applied to contacts on the film edge. With high applied voltages, the change in index of refraction and the spectral shifts should appear much more distinctively than with these low voltages. The data similarities between 1000V and 1500V indicated a saturation of the effect, in contrast to the GaScN films discussed below. Although preliminary in that this effect was observed in only one film, the result is promising in making an electrically-controlled smart active optical device.

In a similar experiment, applying the same voltages to a thin-film of Sc-doped GaN ( $\text{Ga}_x\text{Sc}_{1-x}\text{N}$ ,  $x=0.47$ ) on a quartz substrate caused both the spectral and refractive index to shift to higher photon energy as shown in Figure 14 and Figure 15. It is also anticipated that the effects of magnetic field (Zeeman effects) on  $\text{Ga}_x\text{Sc}_{1-x}\text{N}$  systems demonstrate both the changes in index of refraction and spectral shifts, but do not saturate at 1000V as with the ScN films. In a recent batch work, the co-sputtered Al and Er in nitrogen/argon atmosphere resulted in a  $\text{AlN:ErN}$  alloy film with the concentration ratio of 80:20. As with the applied bias effect these results are preliminary; however, this sample shows the strong evidence of possible field induced optical constant shifts. It is noteworthy that narrow bandgap materials offer a wide spectral controllability, allowing fine adjustment of optical information with minute field strength.



**Figure 10. Index of refraction in the region below optical absorption. Data generated from variable angle spectroscopic ellipsometry (VASE).**

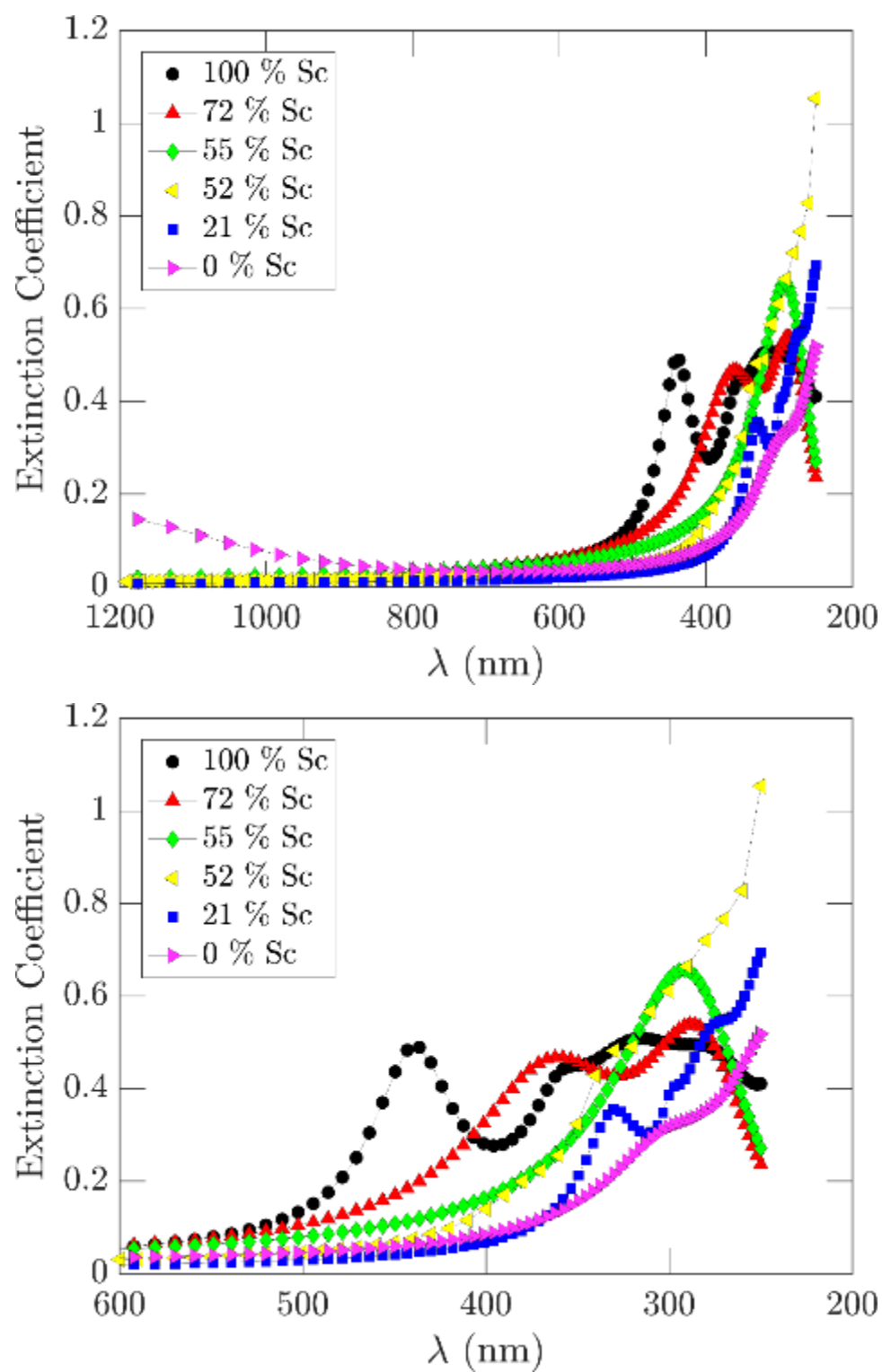


**Figure 11. Extinction coefficient  $\kappa$  from VASE over the (top) full test range and (bottom) 200-600nm range to clarify behavior.**

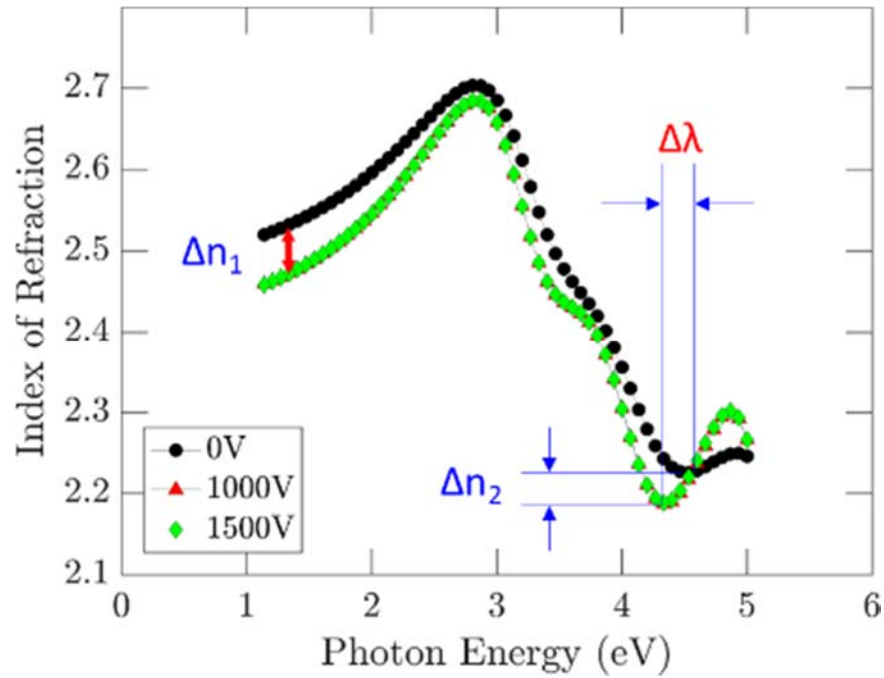


**Figure 12.** ScN film shows both the spectral ( $\Delta\lambda$ ) and refractive index shifts ( $\Delta n$ ) very clearly from 2.7eV to higher photon energy. The electric field was applied with a few mm gap.

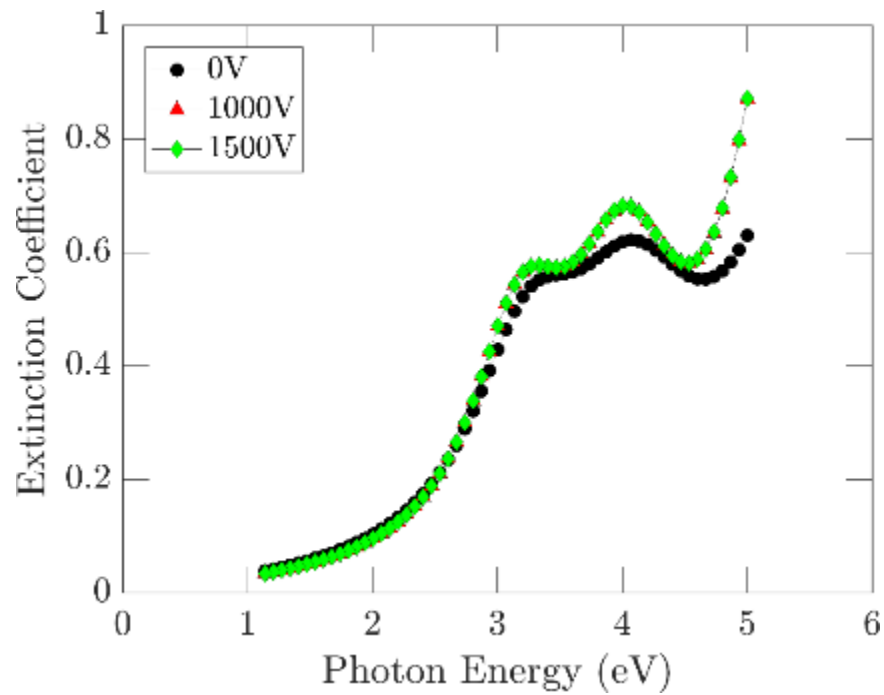


**Figure 13.** ScN film shows the change in the extinction coefficient with the applied electric field. The electric field was applied with a few mm gap.

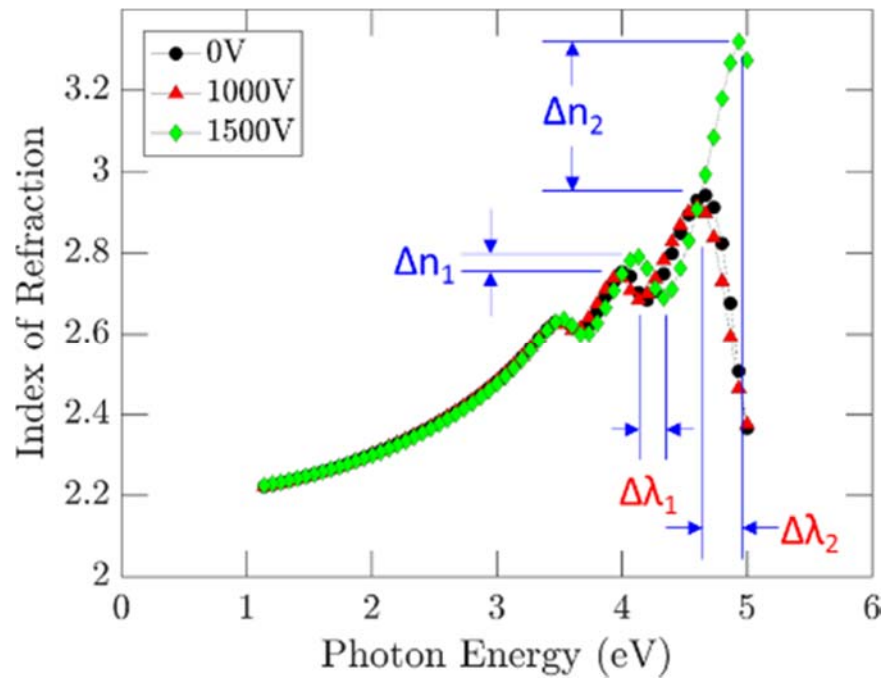


Figure 14. Spectral and refractive index shifts of thin film  $\text{Ga}_x\text{Sc}_{1-x}\text{N}$  ( $x=0.47$ ) on a quartz substrate.

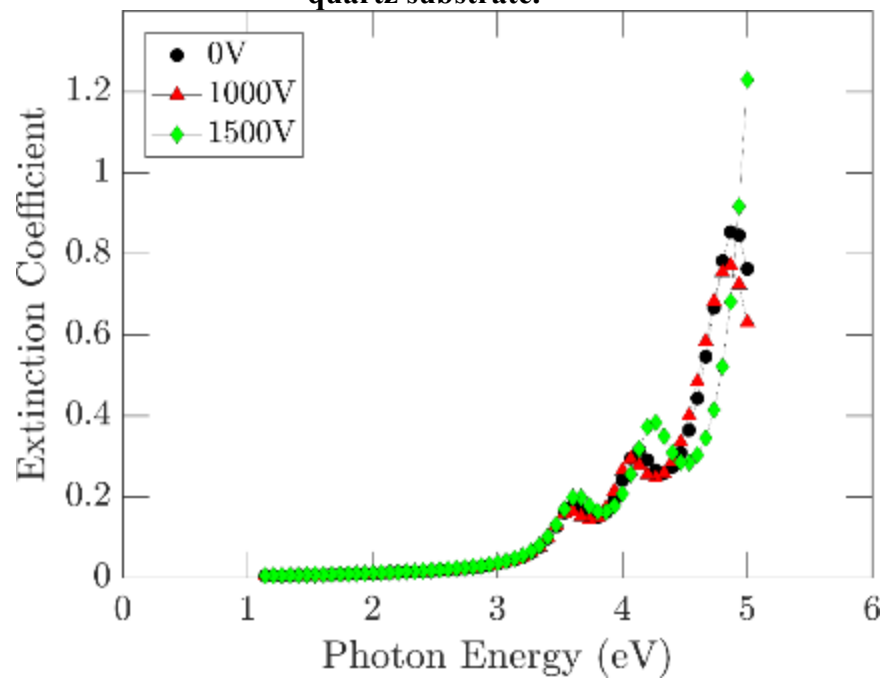
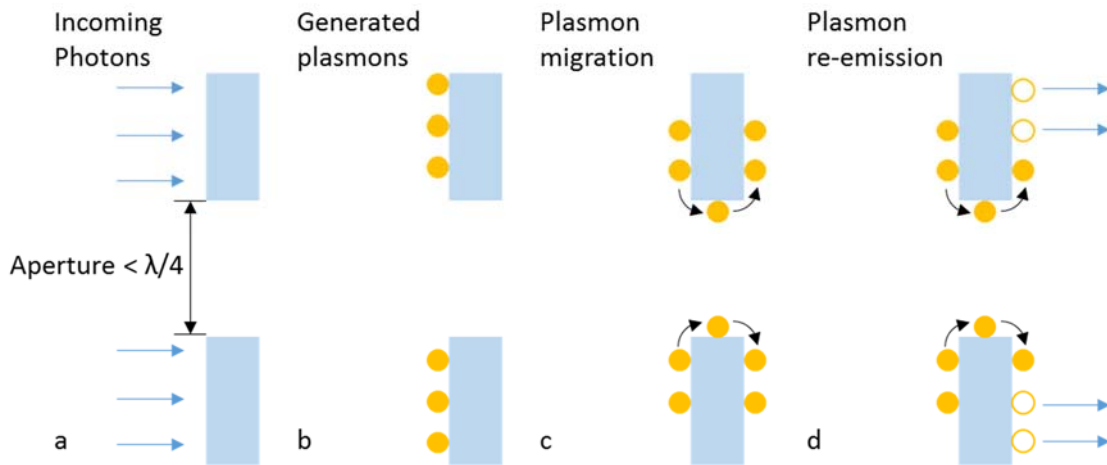


Figure 15. Extinction coefficient data of thin-film  $\text{Ga}_x\text{Sc}_{1-x}\text{N}$  ( $x=0.47$ ) on a quartz substrate.



### II-3. Wavelength Dependent Transmission Through Nano-apertures

When incident photons are coupled with the motion of surface plasmons (the quantized motion of collective electrons on the metal surface), tiny apertures in metal layers show unusual electro-optical effects and the extraordinary transmission of long wavelength photons. According to the classical electro-magnetic theory, when tiny apertures have diameters smaller than  $\frac{1}{4}$  of the wavelength of electro-magnetic waves, they do not transmit the electromagnetic waves. Nevertheless, Ebbessen et al. showed long-wavelength photons, even wavelengths up to 9 times the aperture diameter, can transmit through the metallic aperture by the coupling with surface plasmons.[41,42] Figure 16 demonstrates this concept. Impinging electromagnetic waves couple with the surface electrons, causing a collective oscillation of electrons. These coupled movement of electrons is known as a surface plasmon polariton (SPP). The SPP propagates not only on the surface metal film, but also over the wall surface of hole as shown in Figure 16. In such a fashion, the SPP carries photon energy through the hole and eventually releases its own carried energy by the momentum change at the edge of hole exit. However, the SPP cannot carry the overall coupled energy of photons due to the losses related to the coupling efficiency of surface plasmons and jittered momentum changes on the exit edge. It is hard to quantify such losses by measurement but the spectral (red) shift of transmitted wave indicate a lossy transmission. Since the SPP can be easily disrupted by electric or magnetic field, it is also possible to modulate or orchestrate the SPP for the desired spectral shift. Such functional control of SPP can be used for many applications, for examples, the on-off switching, dimming, and spectral selection of optical light transmitted through the array of holes, backlit flat-panel displays, optical diodes, variable gratings and filters, surface plasmon resonance (SPR) spectroscopy, optical windows for sensors and probes, sub-wavelength photolithography, Raman spectroscopy, and monochromators.



**Figure 16. Extraordinary Transmission of EM Waves through Nano-Aperture by surface plasmon polariton (SPP).**

Also, Ebbessen et al. reported that the extraordinary transmission can only occur in the ultra-pure metal surface with plasmons.[41,42] Focused ion beam (FIB) lithography is an attractive tool to create precise nano-scale holes, but has a size limit for array of holes. As an alternative, electron beam lithography can write a large pattern array of nano-apertures, but lacks selective etching



capability. Holes with identical diameter and edge shape are necessary for a uniform response to incident electromagnetic waves. Besides the size limit of FIB, nano-patterning by FIB has very high aspect ratio of 1:10 or better and it supports in-situ monitoring with Secondary Electron Microscopy (SEM) during the ion-beam etching process. The left picture of Figure 17 shows the cross-section view of thin-film structure. Thin films of gold (Au) and electro-optical (EO) material are built on sapphire substrate sequentially. The conductive film of indium-tin oxide (ITO) is coated at the bottom of sapphire to feed a control signal to the EO layer and the SPPs on the gold film surface. The right pictures of Figure 17 show the SEM images of fabricated nano/quantum-apertures of various diameters from 60nm to 200nm.

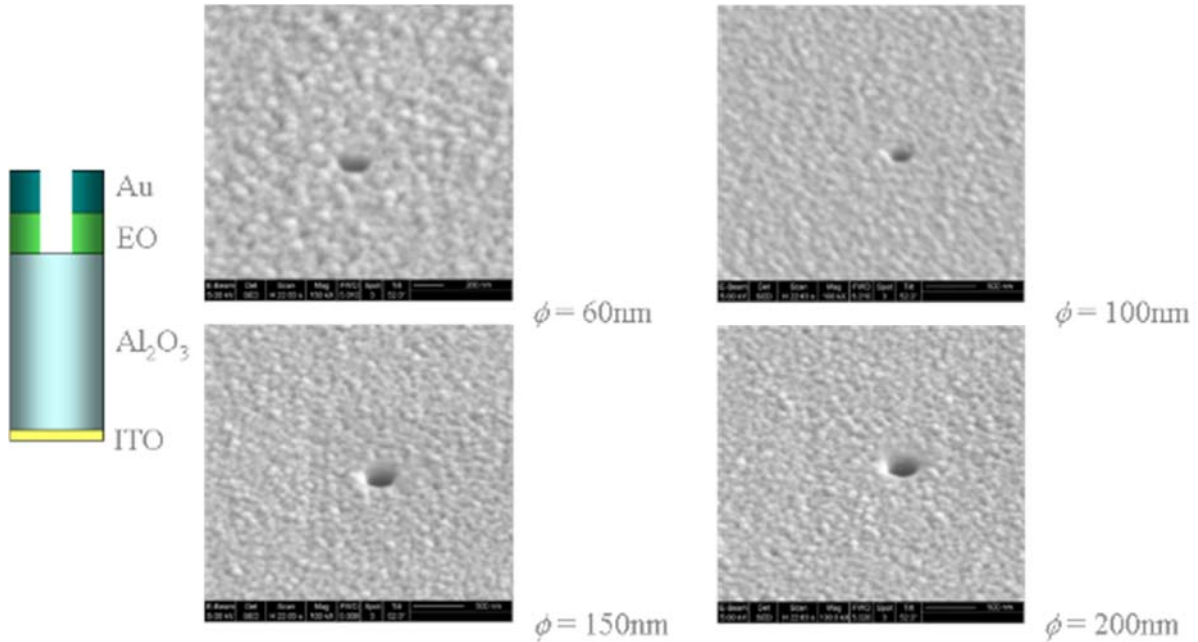


**Figure 17. (Left schematic) Cross-section view of thin film, (Right pictures) SEM images of fabricated nano-apertures with various diameters.**

Arrays of  $12 \times 11$  nano-apertures were also fabricated as shown in Figure 18. Each hole has a 100nm diameter and 400nm depth. Among 132 apertures, four holes were selected for enlargement with double-writing of focused ion beam so that they have 150nm diameter and 800nm depth. These 150nm apertures were for a comparison of the effect of aperture diameters.

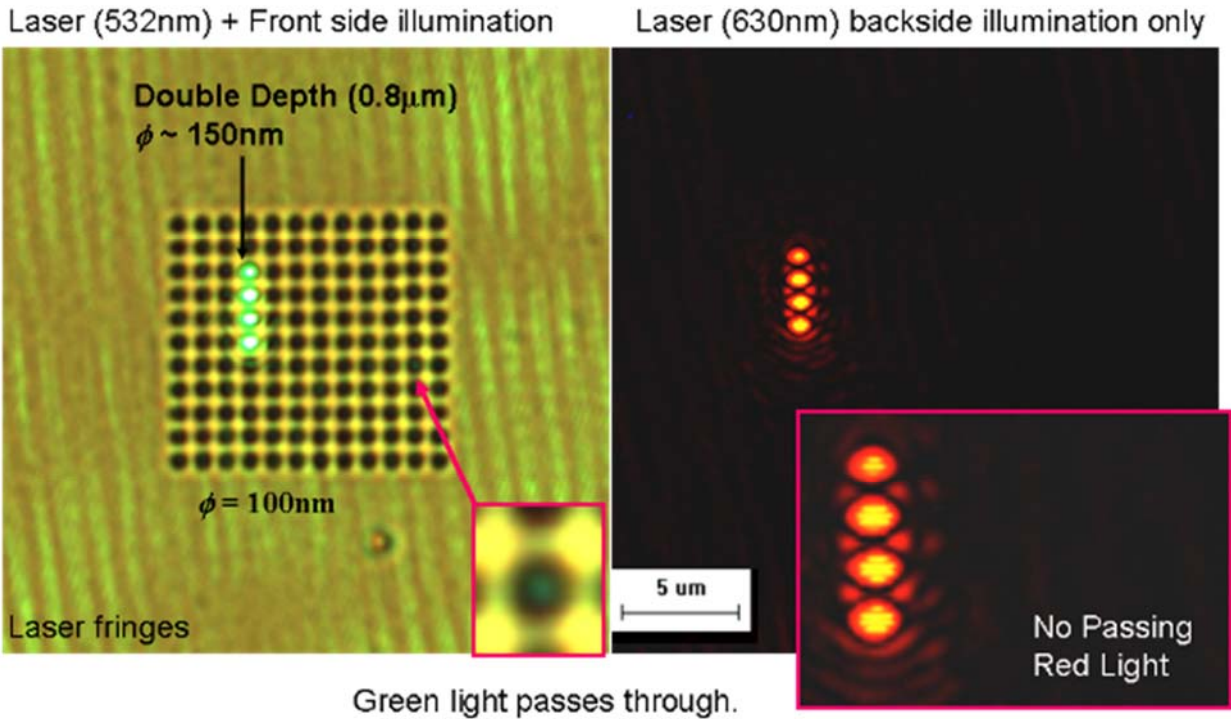


**Figure 18. (Left) Transmission of green laser (532nm) through nano-apertures of 150nm and 100nm diameter, (Right) Transmission of red laser (630nm) is blocked in nano-apertures of 100nm diameter.**

Green (532nm) and red (630nm) lasers were used for the measurement of optical transmission through nano-apertures. The left picture in Figure 18 shows a microscopic image of transmitted green lasers through nano-apertures. Four bright spots indicate highly efficient transmission of 532nm photons through 150nm holes and the inset-picture shows attenuated transmission through the 100nm holes. The right picture in Figure 18 shows the transmission of 630nm photons. The four large 150nm holes allow a large transmission of photons but the 100nm holes do not have any measurable transmission of red color light. Therefore, this test results show that a threshold of optical transmission through nano/quantum apertures occurs when the diameter of aperture is approximately  $\lambda/4$ . This proves the technique is effective in transmitting light through apertures too small for conventional light transmission through a hole. However, the conversion of photons to polaritons, transmission losses, and then reconversion of polaritons into photons involves many efficiency penalties.

Nano-apertures will be used as the pixel defining array in the complete system to achieve hyper-spectral sensing and imaging with the following micro-zone-plate (MZIP) technology because we can easily utilize the threshold diameter,  $\lambda/4$ , in order to control the light source. Likewise, the transmission of light through quantum-apertures can be tailored for the variety of applications. Applied voltage can affect the polariton transmission and diffraction behavior of the apertures, allowing easy control of the subsequent light re-emission wavelength. This allows many useful applications, such as the on-and-off switch of Figure 19 for optical diodes, dimming and spectral selection of optical light transmitted through the array of holes (Figure 20), backlit flat-panel displays, variable gratings and filters (and Figure 21), surface plasmon resonance (SPR)

spectroscopy, optical windows for sensors and probes, sub-wavelength photolithography, the Raman spectroscopy, the monochromators, and near-field scanning microscopes.

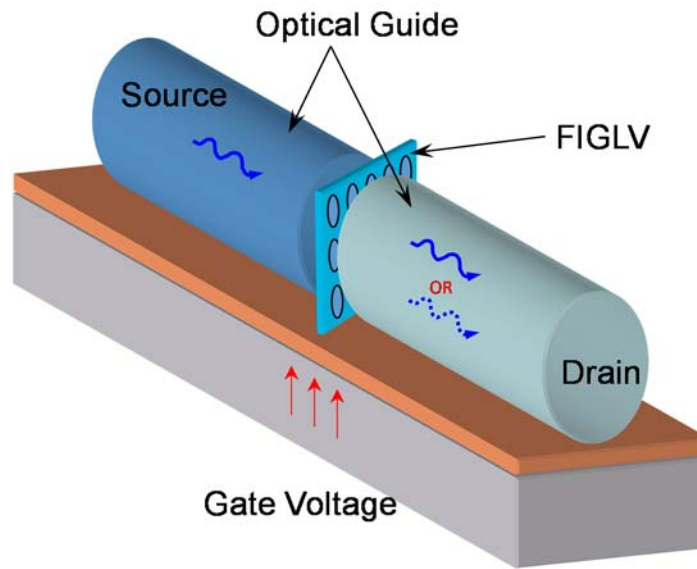


**Figure 19. Field Injection Grating Light Valve (FIGLV) optical diode concept. Light from a source is passed through an array of quantum-apertures, allowing only a particular wavelength through to the drain. The substrate acts as the gate, where an applied voltage disrupts polariton migration, changing the transmitted wavelength.**

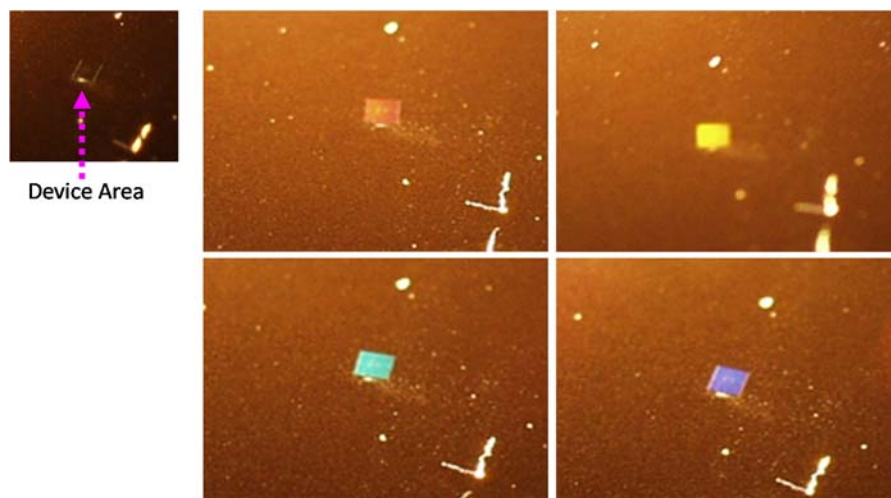


**Figure 20. Examples of color selection capability through quantum-apertures, where an applied bias alters the diffraction behavior, resulting in color selectivity.**

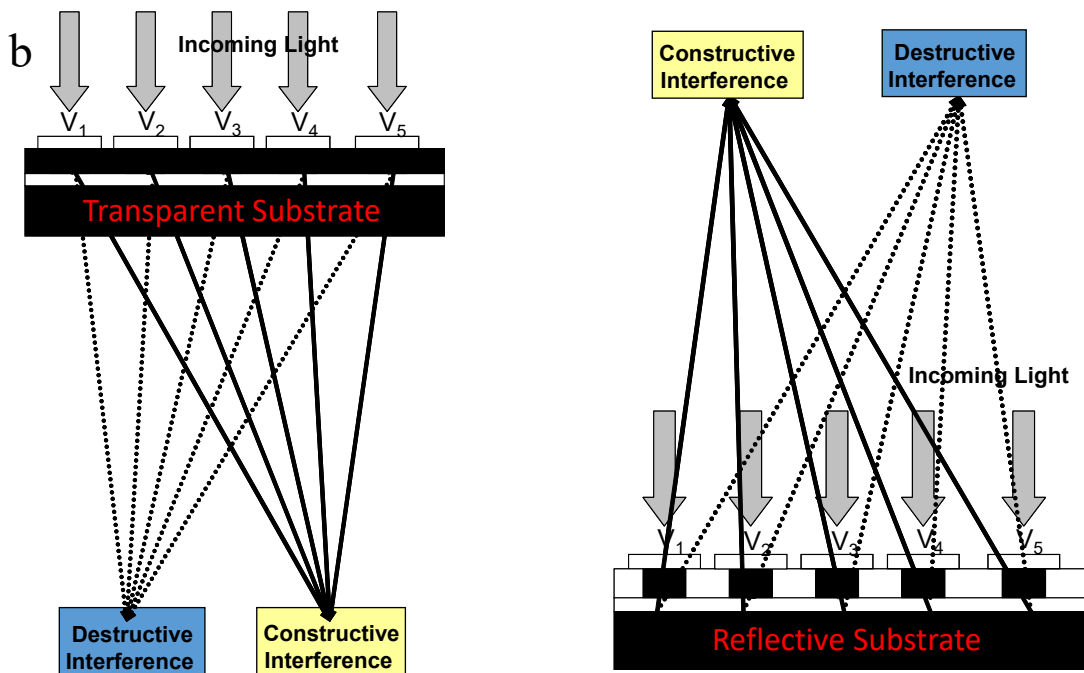
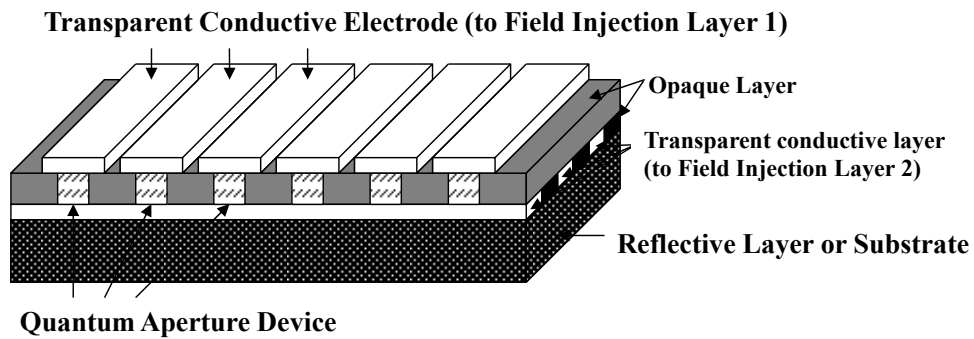
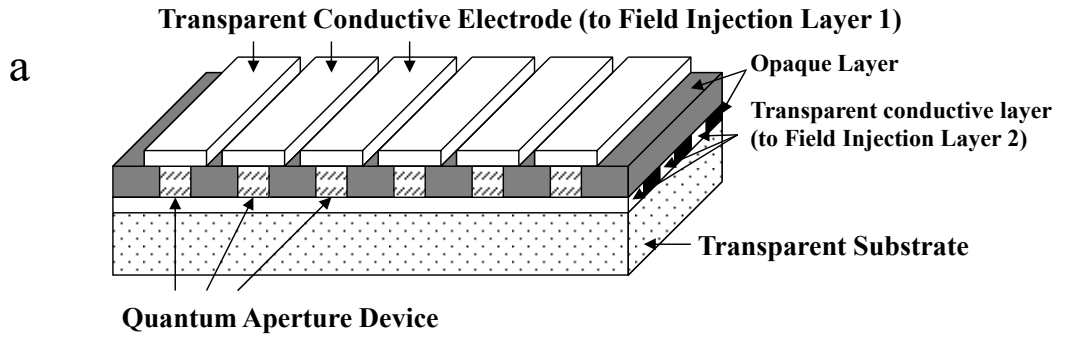
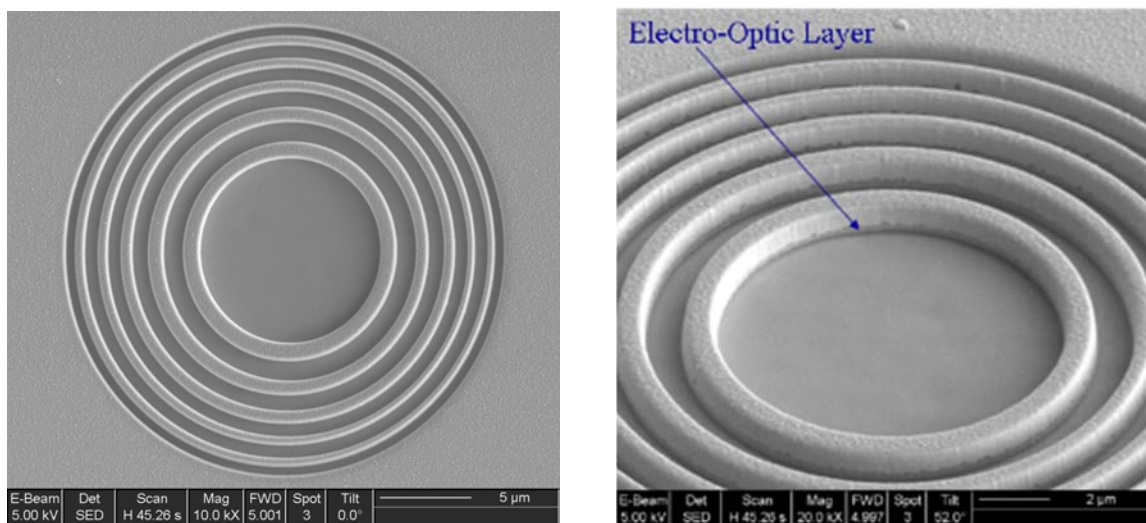


Figure 21. (a) Quantum-aperture as a pixel controlled for spectral selection and interference images. Top: transmission device concept. Bottom: reflection device concept. (b) Selective wavelength focusing concept. The  $V_1, V_2, \dots, V_5$  notation indicates the applied bias on that aperture of the device.

Figure 21 describe the field-controlled device concept for focusing a specific wavelength on any desired location. As such, this device is capable of differentiating between spectral signatures from multiple sources. Each source is split into its spectral lines as the photons pass through the apertures. This permits high resolution measurement of optical data. One possible application exists in space optics. Many chemical or physical signatures are bundled together as they reach the sensor plane. In order to identify each spectral signature, the data must be further resolved using a complex monochromator. The device shown in Figure 21 is capable of directly resolving each signature without the need for complex optical paths and a monochromator. Different electric and/or magnetic field on each quantum hole device results in the different index of refraction for (left) transmission and (right) reflection. Therefore, the exit photons have different phases, depending on the applied electric and/or magnetic field.

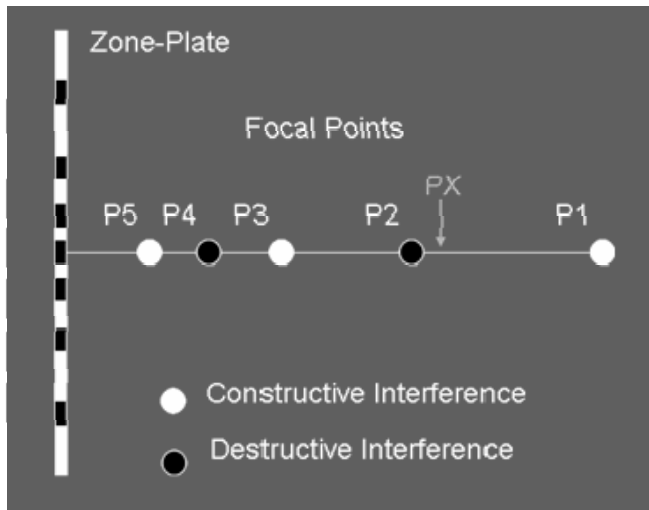
#### II-4. Micro Zone Plate Technology for Programmable Lens



**Figure 22. (Left) Fabricated Micro Zone Plate, (Right) Transparent electro-optic layer and metal rings.[43,44]**

The electro-optic micro-zone-plate (MZIP) is shown in Figure 22.[43,44] The rings are made of Au and the transparent region is made with electro-optic layers of BaTiO<sub>3</sub> and LiNbO<sub>3</sub>. A conventional zone-plate consists of concentric blackened-rings with non-linear pre-calculated diameters. Figure 23 shows the multiple calculated constructive and destructive focal points of the fabricated MZIP in Figure 22, including a previously undiscovered point PX caused by a phase-contrast mechanism such that destructive interference ring surrounds and sharpens the constructive focal spot at center.





### Estimated Focal Points

**P1 = 46.99  $\mu\text{m}$ , Constructive**

**P2 = 15.66  $\mu\text{m}$ , Destructive**

**P3 = 9.40  $\mu\text{m}$ , Constructive**

**P4 = 6.71  $\mu\text{m}$ , Destructive**

**P5 = 5.22  $\mu\text{m}$ , Constructive**

Figure 23. Estimated focal points (P1~P5) of MZP and location of newly discovered pseudo-focal point PX.

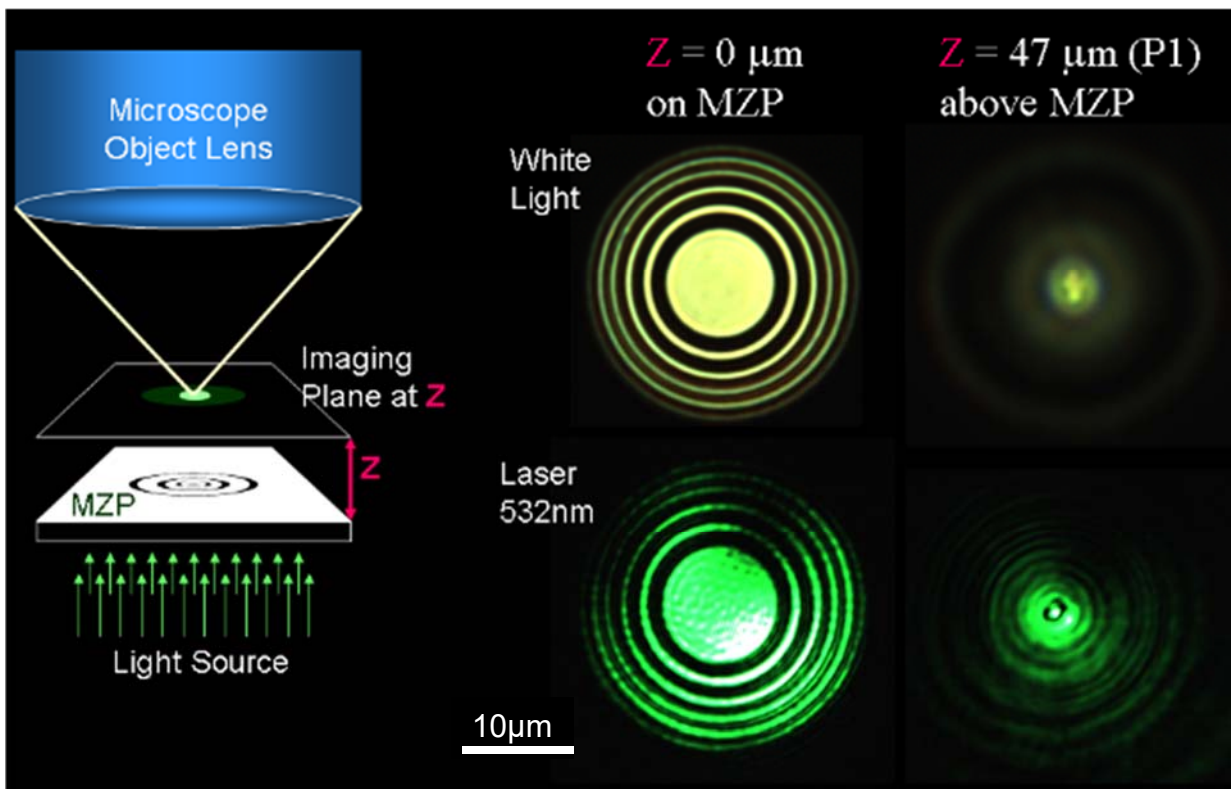


Figure 24. (Left) Experimental configuration of imaging plane above MZP, (Right) Acquired photon distribution on imaging plane at  $Z=0$  (MZP itself) and  $Z=P1$  (1st focal point) from white light source (light bulb) and green laser (532nm).

The fabricated MZP is about 20 $\mu\text{m}$  in diameter and the longest focal distance is less than 50 $\mu\text{m}$ . This small size and short focal length has great promise in miniaturized system construction. Also, the MZP above has additional electro-optic layers where refractive index varies with applied

electric field. These features add versatility and programmability to the MZP and makes it the world's smallest programmable micro-lens and micro-ring-grating.

The MZP performance was tested with a microscope as shown in the left picture of Figure 24. The height ( $Z$ ) of the imaging plane was changed to reveal the distribution of photons on the imaging plane at each  $Z$ . The photon distribution on the imaging plane was recorded with CCD detectors on the microscope. The right pictures in Figure 24 show photon distribution at different  $Z$  heights,  $Z=0$  on the MZP itself and  $Z=47\mu\text{m}$  (1st focal point P1). The upper data is from a white-light-source (common light bulb), and the lower data is from a monochromatic green laser (532nm). The scale-bar at the center-bottom is  $5\mu\text{m}$ .

The sharpness of the P1 and PX central spots are shown in Figure 25. The data at P1 and PX were obtained with 4ms and 6ms of CCD exposure time respectively so that the full width at half-maximum (FWHM) values are comparable. FWHMs of the central focal spots were 620nm at P1 and 465nm at PX. It is surprising that large amounts of photons can be focused below its wavelength ( $\lambda=532\text{nm}$ ). The reduction in focal spot diameter has many important applications. For example, if a 1 milliwatt laser was focused on the focal spot at PX, its power density would be  $10^5\text{ Watt/cm}^2$ , powerful enough to melt anything in this tiny point. Because there is a great importance in the phase-contrast pseudo focal point PX, applications of PX have been dubbed “Photonic DART” (Densely Accumulated Ray-point by micro-zone-plaTe) technology.[45] Moreover, the MZP can work as a microconcave lens when the height of imaging plane is negative ( $Z<0$ ). For imaging planes below  $Z=0$ , the CCD image shows a virtual focal point P(-1) at  $Z = -47\mu\text{m}$ , indicating operation as a concave lens.

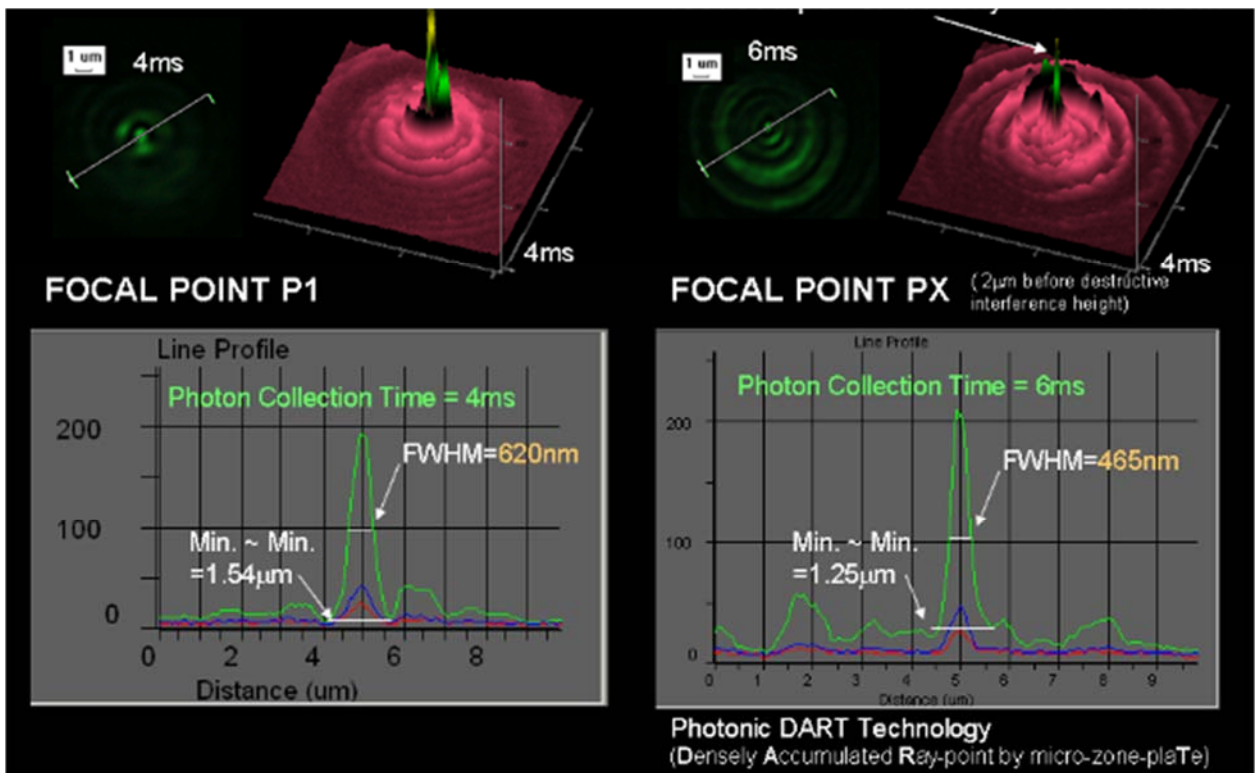


**Figure 25. Comparison of sharpness of focused beams at  $Z=P1$  (left) and  $Z=PX$  (right).**

#### II-4-1. Applications of Programmable Micro-Lens

The programmable micro-lens based on the MZP configuration enables the construction of tiny spectrometers using the principle of Fresnel diffraction.[46,47] Miniaturization of spectrometers offers many interesting applications, such as a neural probes and soil assay probes for on-site, real time analysis of Lunar or Martian soils.[47]

The device concept for micro-spectrometers is based on programmable micro-lens as shown in Figure 26.[48] When an electric field is applied upon the MZP thin film structure, it generates a circular gradient refractive index in the electro-optic layer and changes the focal distance. The fabricated MZP shown in Figure 22 has the electro-optic and transparent electrode layers. In photonic DART technology, phase-contrast sharpening of the focal spot has many applications. An array of photonic DARTs can be used for maskless phase-contrast (PC) lithography with MZP.[48] Conventional PC lithography requires fabrication of an expensive PC photomask for each pattern, whereas MZP-based PC lithography avoids this problem. This technology uses X-Y scanning of phase-contrast focal points (multiple PX points) which are made from an array of MZPs. The full MZP lithography system can be constructed with or without electro-optic layers.

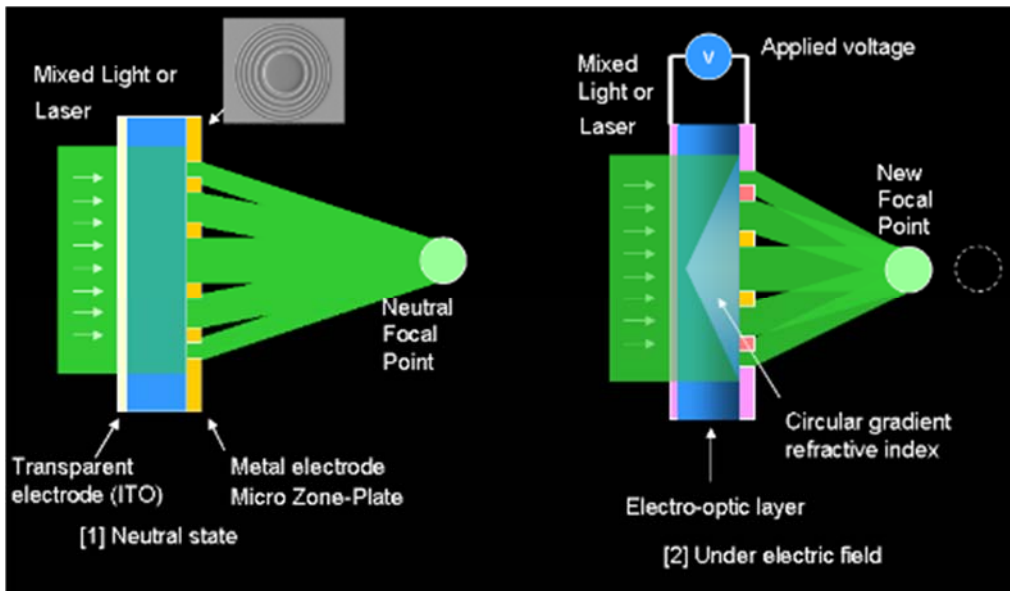
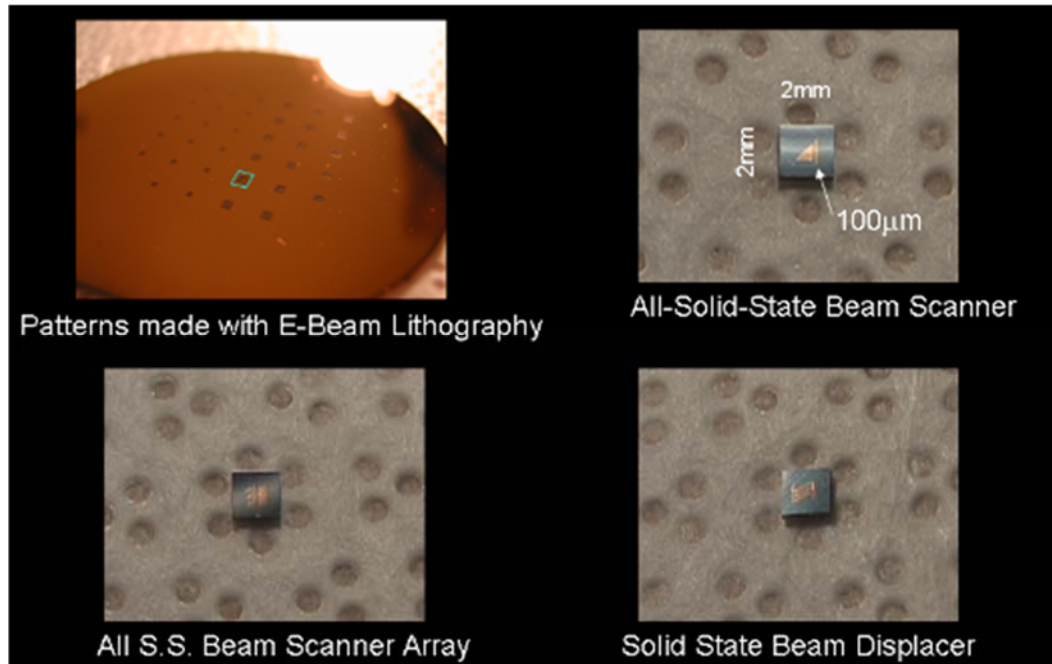


Figure 26. Programmable Micro-Lens.[48]

#### II-5. Solid State Beam Scanner Micro-chips

Solid state beam scanner micro-chips were developed in order to characterize the electro-optic materials without the large errors and uncertainty of ellipsometry. Figure 27 shows the fabricated micro-optical devices, a single beam scanner, the beam scanner array, and the beam displacer. The size of each device is 2mm×2mm×0.5mm.





**Figure 27. Fabricated Solid-State Beam Scanner Micro-chips.**

Light is injected into a waveguide from the side of the chip and electric field is applied to the triangular and diagonal-bar shaped electrodes. Three different modes are shown in Figure 28. When light encounters a media of different refractive index, the propagation direction changes according to Snell's law. Because a part of the electro-optic waveguide is under electric field and other parts are free from electric field, an interface of two different refractive indices occurs and the laser beam is bent. By measuring the bending angle of laser beam, the change of refractive index by e-field is characterized absolutely. To test this, Eu-doped BaTiO<sub>3</sub> thin-film was deposited onto a substrate as an electro-optic wave-guide layer. Because BaTiO<sub>3</sub>:Eu was reported to show room-temperature photo-luminescence and electro-luminescence, it is likely able to amplify the passing laser of a specific wavelength by electric pumping.[37]

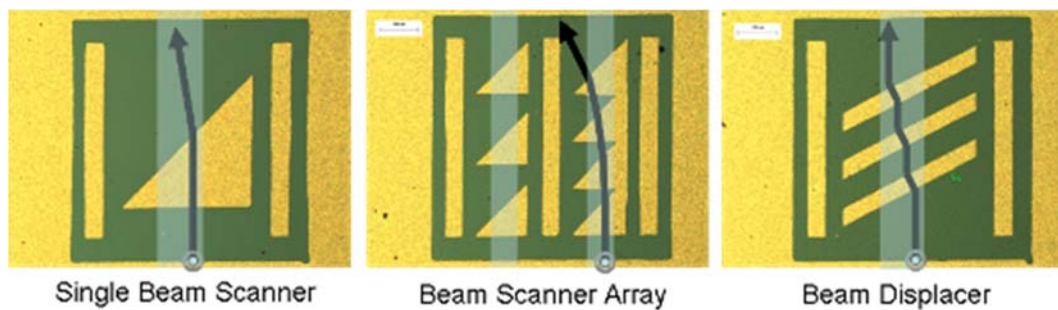


**Figure 28. Operating Modes of Various Solid-State Beam Scanner Micro-chips.**

Figure 29 shows the wave-guide device under optical test. At each stage, the beam deflected  $0.2^\circ$  for an applied excitation voltage of  $\pm 15\text{V}$  at frequencies from 1-10 Hz, but higher frequencies up to a GHz are theoretically possible. In order to achieve a  $30^\circ$  deflection, about 150 stages are required, well within standard microelectronic fabrication techniques. When the light enters a media of different refractive index, a small portion of light is reflected backward. When the number of stages is increased, the intensity of propagating light is attenuated rapidly due to the cumulative small reflections. To mitigate this problem, the waveguide can be built out of an electrically amplifying material and the final exit light amplified by electric pumping.  $\text{BaTiO}_3\text{:Eu}$  described above can serve this purpose.

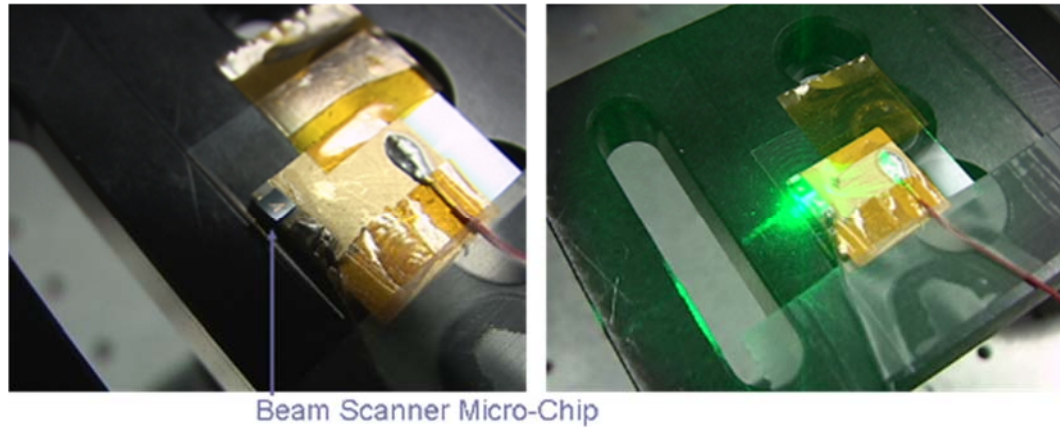


**Figure 29. Performance test of solid-state beam-scanner micro-chip (Left) without illumination, (Right) with green laser passing through.**

### **III. Tunable lenses**

#### **III-1. Tunable liquid lenses**

Tunable-focus liquid lenses play an important role in modern miniaturized optical systems, bio-inspired visions, optical communication systems, and consumer electronics. The liquid lens varies its focal length by changing either the refractive index or the curvature of liquid droplet or liquid-liquid interface without the need for mechanical actuators. These lenses are small in volume, simple in structure, and consume much less power for control as compared to conventional solid lens modules.[49] A liquid lens fabricated on a flexible substrate can be wrapped onto any curvilinear surface, providing more advantages in expanded field of view and reconfiguration capability. There are several methods used for adjusting the focal length of a liquid lens, including thermal,[50,51] fluidic pressure,[52,53] electro-wetting,[54–56] electromagnetic wave and dielectrophoretic (DEP),[49,57–59] and electrostatic effects.[60,61] Each method has its own advantages, but some drawbacks exist for many of these approaches. Long response time and thermal effect are usually associated with hydrogel actuators. Electro-wetting using conductive liquids could cause undesirable Joule heating and microbubbles resulting from liquid electrolysis. Liquid crystals could cause images to be blurred below its transition temperature. Acoustic wave methods are ill-suited for maintaining a specific focal length. Fluidic pressure needs external pressure sources for the focus-tuning. Compared to these methods, the DEP effect uses two non-conductive liquids achieve small volume, fast response low power consumption, and avoids

electrolysis owing to the negligible current in the liquids. Using the DEP effect, conventional dielectric liquid lenses (DLLs) have been built on a flat and rigid substrate, such as glass, silicon, or polyethylene terephthalate.[57,58] Figure 30 (left side) shows a demonstration of a DLL formed on a rigid substrate. The DLL consists of a low dielectric constant droplet and a high dielectric constant sealing liquid. The two non-conductive liquids are sealed in a chamber under iso-density conditions. Focal length of the DLL with an aperture of 3 mm can be changed from 34 mm to 12 mm as the input voltage increases from 0 to 200 V. Focal spot size is approximately 80  $\mu\text{m}$ , while rise and fall times are 650 ms and 300 ms, respectively. During operation with 200 V at 1 kHz, the lens consumes 1 mW of power. The longitudinal and transverse spherical aberrations are estimated to be nearly invariant when the focal length exceeded 20 mm.

Recently, owing to improvements in metal film adhesion to polymer substrates, the DLL may be fabricated on flexible and curved substrates. [49] Figure 30 (right side) shows demonstration of a DLL made on a flexible polydimethylsiloxane (PDMS) substrate. As a positive meniscus converging lens, the DLL has the focal length variable from 14.2 to 6.3 mm in 1.3 seconds when the driving voltage increases to 125 V<sub>rms</sub>. The resolving power of the DLL is 17.95 line pairs per mm. [49]

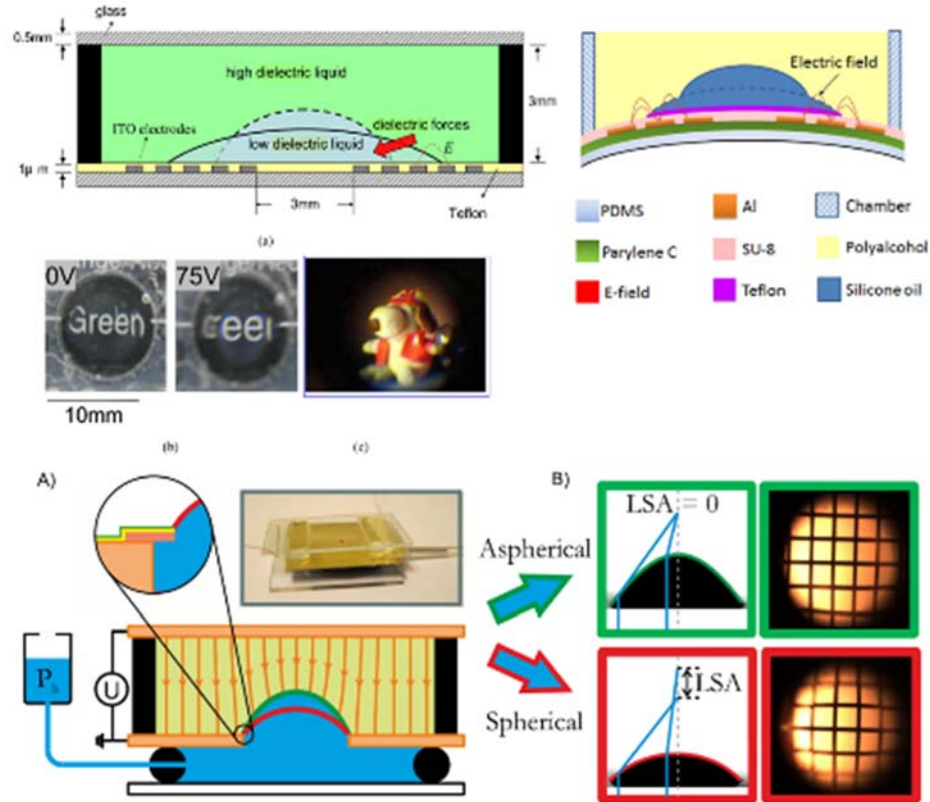


**Figure 30. DLLs using rigid (Top-left) and flexible substrate (top-right) and widely-variable focus that is possible in the optic system(bottom).[49,58,60]**

Although these adaptive liquid lenses enable widely-variable focus in optical system, the lenses commonly suffer from packaging problems, gravity effects, and substantial spherical aberration that compromise the optical performance of the system. To resolve the packaging problem, a

polymer-encapsulated liquid tunable lens was developed by directly depositing parylene on liquid droplets in vacuum.[61] The polymer coating contributes to preserving the shape of the delicate spherical droplets, prevents the loss of liquid, and protects the droplets from ambient conditions. The polymer is also extremely thin and flexible, it allows the droplets to deform. Electro-static force changes the shape and thus the focal length, but this requires a thin metallic layer on the polymer surface to generate the electro-static force, limiting optical transparency of the lens. To suppress spherical aberration and simultaneously modulate both focal length and asphericity, a novel adaptive liquid lens is introduced.[60] The liquid lens achieves superior optical performance by varying both hydrostatic pressures and electric fields to control the interface between an electrically conductive lens fluid and a non-conductive ambient fluid. Continuous variation from spherical interfaces at zero electric field to hyperbolic ones with variable ellipticity for finite fields allows lenses to take on positive, zero, and negative spherical aberration, while the focal length can be tuned via the hydrostatic pressure. Some drawbacks to this approach include the delicate nature of the lens; its thin polymer shell renders it vulnerable to damage from repeated cycling and external force. Moreover, the liquid inside is unsuitable for vacuum, space, and other extreme environments.

### **III-2. Tunable polymer lenses**

Electro-active polymer (EAP) is an emerging class of smart material. Tunable lenses made with EAP are able to respond to mechanical, magnetic, optical, thermal, chemical, electrical or electrochemical stimuli. As tunable polymers, they have enormous potential in the areas including biomimetic robotics, medical robots, underwater robots, sensors, actuators, motors, generators, and speakers. Various EAPs have been developed during last two decades: piezoelectric polymers, ionic polymer metal composites (IPMC), carbon nanotubes, conducting polymers, shape alloy polymers, electro-active gels and bio-based electro-active materials such as cellulose and chitosan.[62–71]

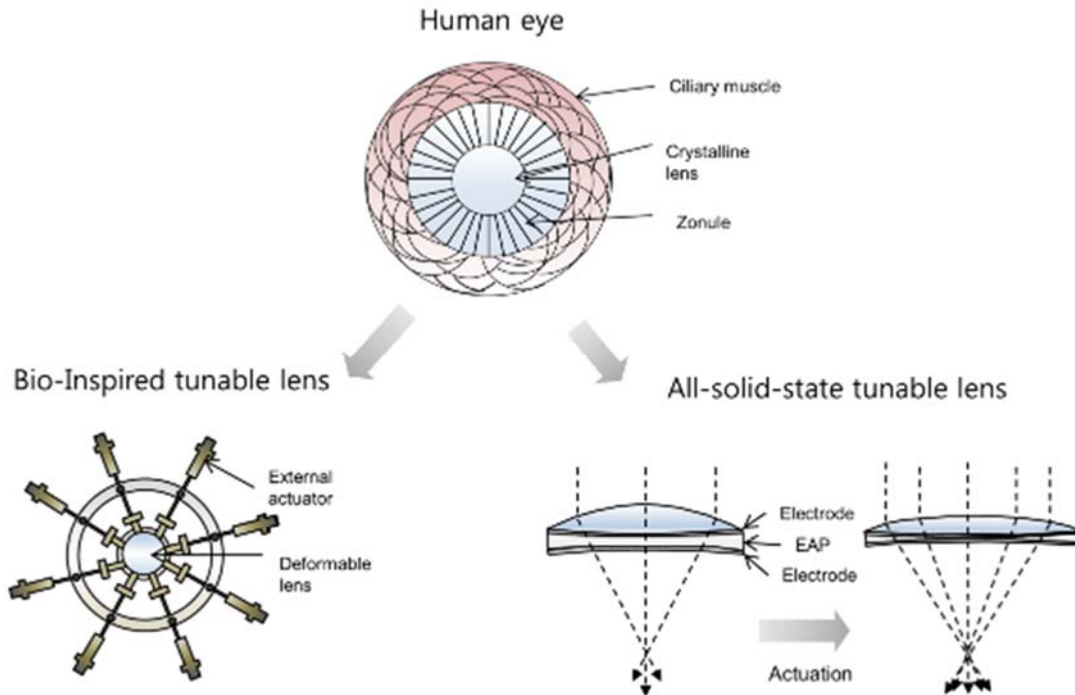


**Figure 31. Two designs of tunable polymer lens that mimic human eye: bio-inspired tunable lens and all-solid-state tunable lens.**

Researchers have attempted to mimic the function of human eye by using the EAPs. Figure 31 shows two distinctive designs of the EAP based tunable polymer lens. The human eye is composed of crystalline lens and ciliary muscle. Similar to this configuration the first design uses stimuli-induced operation of several actuators surround a deformable lens to modulate geometrical shape of the lens, which is called “bio-inspired tunable lens.” EAPs are promising candidates to function like ciliary muscles. However, in realizing the bio-inspired design, stability of lens material against repetitive deformation and miniaturization of the surrounding actuators should be carefully considered. Another design consideration is discoloration or loss of transparency from repeated exposure to light, especially UV and higher energy light.

The second design uses the EAP to directly deform a lens structure or to be a morphing lens itself in the presence of electric field, known as an all-solid-state tunable lens. However, in realizing the all-solid-state design, the EAP coupled to its compliant electrode should possess high optical transparency and produce large deformation with fast response under low voltage. To meet these demanding requirements, several innovative designs for tunable polymer lens have been proposed by utilizing combinations of liquids, EAPs, and novel structural designs.

### **III-2-1. Bio-inspired tunable lenses**

Variable-focus lens systems are one biomimetic copy of the human eye. Figure 32 shows a prototype of the lens system which consists of a PDMS lens, winding-type SMA actuator, and load arms. The PDMS lens is encircled and stretched by the load arms joined to an outer ring that is rotated by the winding-type SMA actuator, thereby changing the focal length of the lens. In contrast to other single tunable-focus lenses, the proposed system uses a gel-type PDMS lens,



which is insensitive to gravity and external vibration, and can be made into a biconvex or aspheric shape. The radius of PDMS lens can be modulated from 6mm to 7mm by activating the SMA actuator.

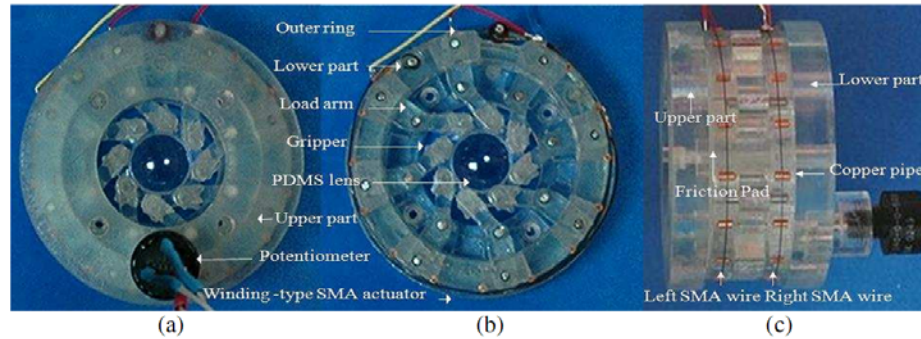


**Figure 32. A variable-focus lens system. (a) Top view, (b) inner structure (c) side view.[72]**

As another bio-inspired approach, an innovative digital camera mimicking arthropod eye has recently been developed.[73] The arthropod-inspired cameras are designed to have hemispherical, compound apposition layouts of arthropod eyes. Figure 33 shows the schematic illustration of the cameras. Their surfaces are densely populated by imaging elements (artificial ommatidia), which are comparable in number (180) to those of the eyes of fire ants (*Solenopsis fugax*) and bark beetles (*Hylastes nigrinus*). The devices are constructed by combining elastomeric compound optical elements with deformable arrays of thin silicon photodetectors into integrated sheets that can be elastically transformed from the planar geometries in which they are fabricated to hemispherical shapes for integration into apposition cameras. The imaging results and quantitative ray-tracing-based simulations illustrate key features of operation. These general strategies seem to be applicable to other compound eye devices, such as those inspired by moths and lace wings (refracting superposition eyes), lobster and shrimp (reflecting superposition eyes), and house flies (neural superposition eyes).

Figure 33a shows an array of elastomeric microlenses arrayed over interconnected silicon photodiodes. When deformed, the lenses form an apposition compound eye camera. The key parameters in this lens are as follows: the acceptance angle (DQ) for each ommatidium, the inter-ommatidial angle (DW), the radius of curvature of the entire device (R) and of an individual microlens (r), the height of a cylindrical supporting post (h), the thickness of the base membrane (t), and the diameter of the active area of a photodiode (d). Figure 33b shows the optical micrographs of four adjacent ommatidia, while Figure 33c shows the lens array after hemispherical deformation. Figure 33d shows the camera system mounted on a printed circuit board. Finally, Figure 33e is an exploded-view illustration of the system: perforated black silicone (black matrix), the microlens array and photodiodes network, thin film contacts, and the black silicone substrate.

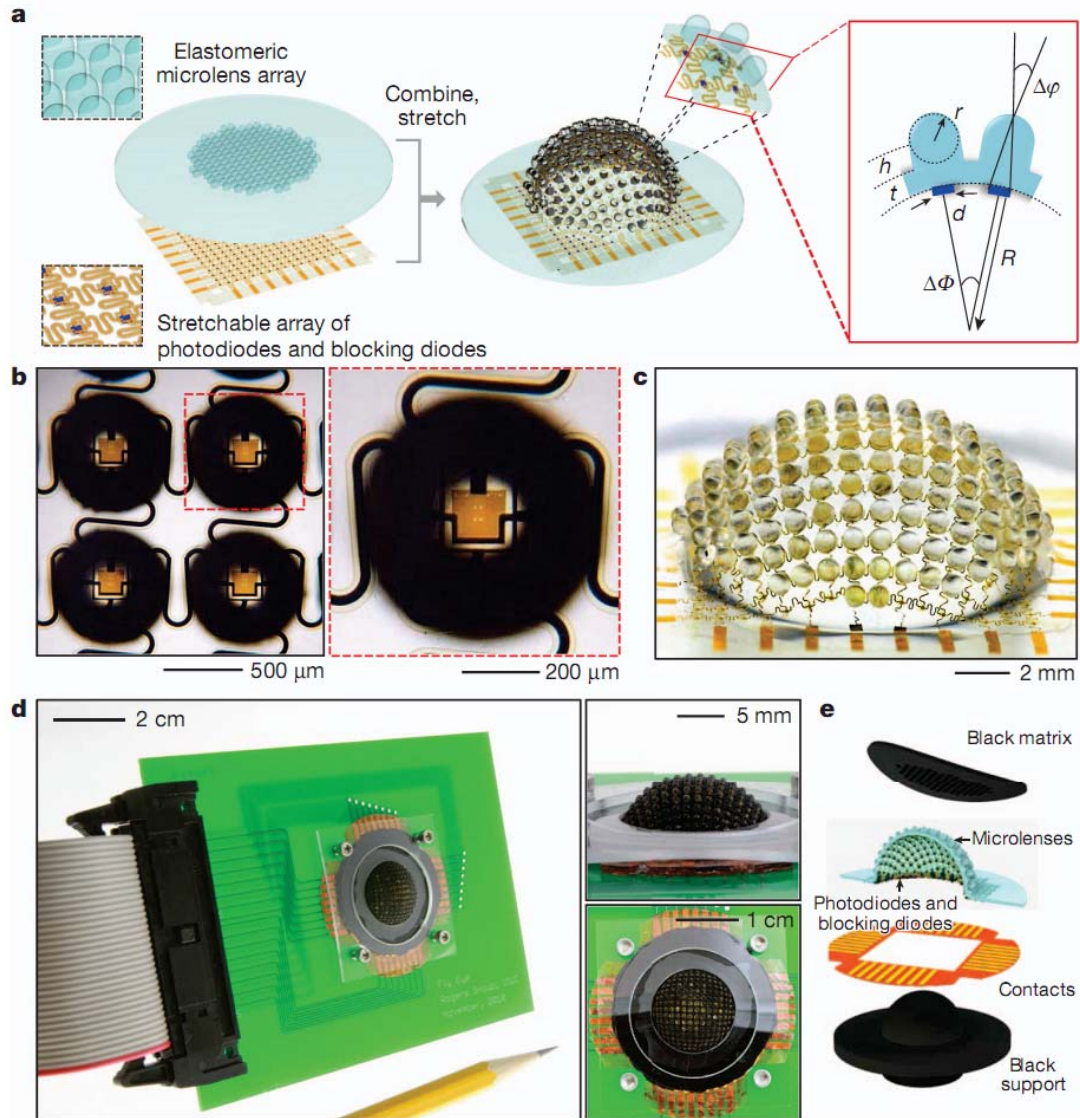


**Figure 33. Schematic of hemispherical, apposition compound eye. [73]**

### III-2-2. All-Solid-State Tunable Lenses

A tunable lens made with all-solid-state materials has been given much attention as one of the candidates overcoming technical difficulties in the liquid based tunable lens, such as packaging, gravity effect, and large-size scalability. The all-solid-state tunable lenses have mainly developed by using optically transparent polymeric materials that can be deformed in response to external stimuli such as pressure or electric field. Figure 34 shows the schematic of a solid-state tunable lens operating with a mechanical pressure. The tunable lens changes its geometrical shape as an elastomeric membrane deforms in response to mechanical compression by a plunger over a distance of  $\Delta L$ , up to a maximum of 1.28 mm.[74] The pressure induced deformation allows its focal length to be reversibly changed by a factor of 1.9. A novel fabrication process based on individual lens components also allows for customization of lens power based on the desired

application. However, this setup is vulnerable to damage if too much force is used, permanently deforming the polymer lens. Design compactness also suffers and shadowing effects from the plunger limit the field of vision.

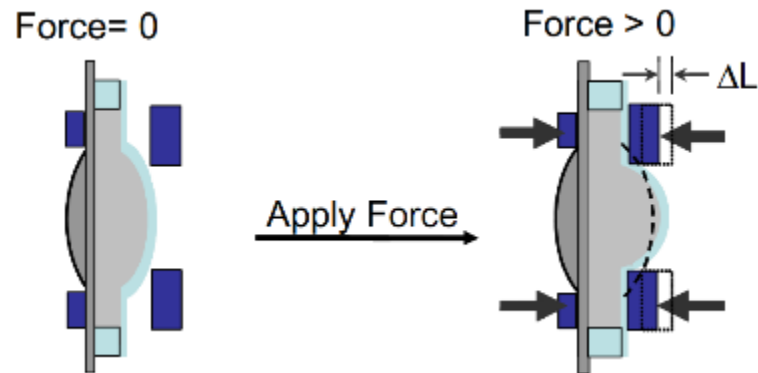


**Figure 34. Schematic of variable focal length in an all-solid state lens.[74]**

As another approach, all-solid-state tunable lenses operating with electric field were developed. The tunable lenses change their focal length responding to self-deformable behavior of electro-active polymers such as gels, nanocomposites and dielectric elastomers. A poly(vinyl chloride) /dibutyl adipate (nPVC) gel based tunable micro-lens was developed.[75]

Figure 35 shows an illustrated operating principle and electrically-induced variable-focusing performance of the electro-active gel based tunable micro-lens. The nPVC gel with a hemispherical plano-convex shape is prepared by bulging the nPVC on an ITO glass as pressurizing an annular PCB structure with a Copper (Cu) electrode toward the nPVC layer. When a voltage is applied to the Cu electrode, electrically-induced creep deformation of the nPVC gel changes its optical focal length. As the voltage increases from 300 V to 800 V, the focal length increases from 3.8 mm to 14.3 mm. Due to its compact, transparent, and electroactive characteristics, the nPVC gel lens can be easily inserted into small consumer electronic devices, such as digital cameras, camcorders, cell phones, and other portable optical devices.



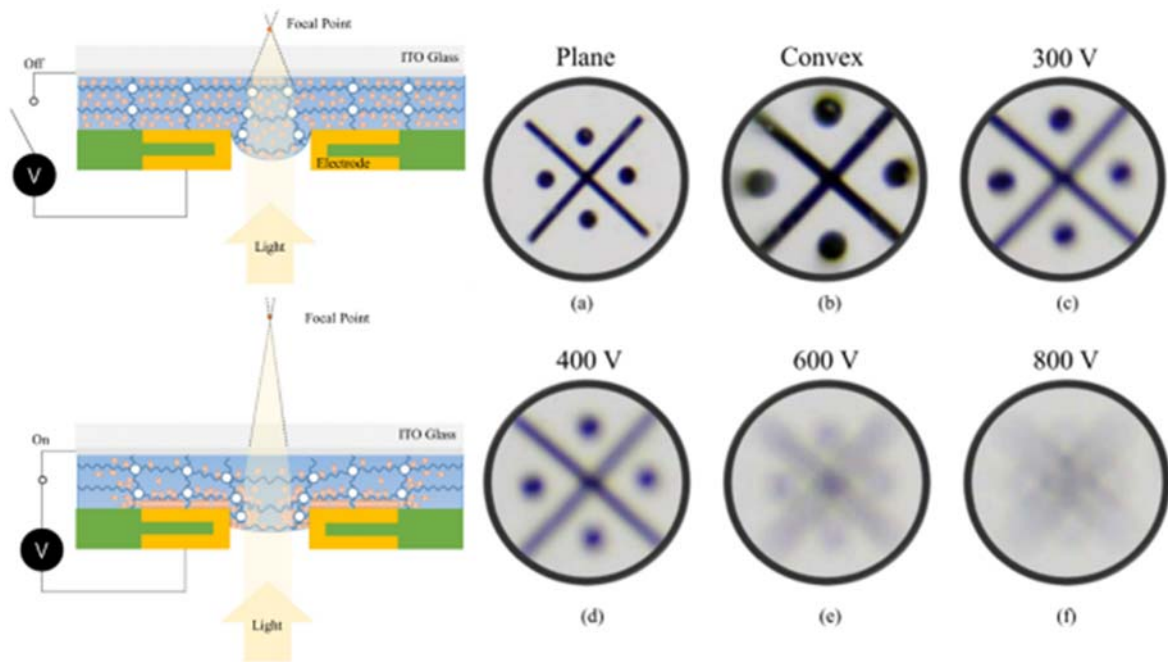


**Figure 35. Electro-active gel based tunable micro-lens.[75]**

A novel electro-active bionanocomposite based tunable lens was developed.[76] The bionanocomposite was composed of poly(diethylene glycol adipate) (PDEGA) and cellulose nanocrystals (CNCs) extracted from cotton. Figure 36 shows a schematic of the bionanocomposite based tunable lens and its focal length change in the presence of electric field. The PDEGA/CNC bionanocomposite possesses high optical transparency, biodegradability and thermal stability. The shape and curvature of the soft PDEGA/CNC lens can be modulated according to voltage signal. The shape reconfiguring performance of the lens is highly durable with low power consumption.

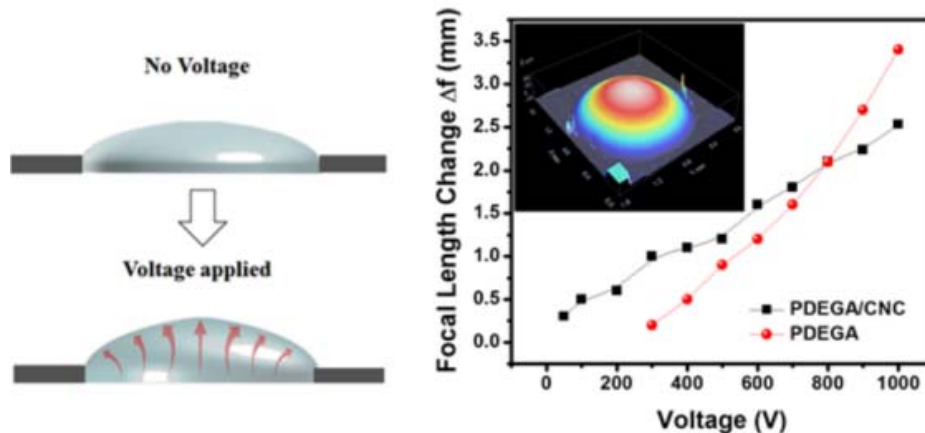


**Figure 36. PDEGA/CNC tunable lens deformation with applied voltage (left) and measured focal length change.[76]**

Due to the benefits from electrically-induced large deformation with rapid response and high optical transparency, the dielectric elastomer has also been considered as an attractive material for

tunable lens. For tunable lens applications, a few approaches using deformation behavior of dielectric elastomers were recently investigated.

A transparent dielectric elastomer actuator driven by few-layer-graphene (FLG) electrode was one such approach.[77] On a silicon elastomer, electrodes were made of graphene, and the transparent actuator was fabricated from developed FLG electrodes (Figure 37). The developed FLG-driven actuator exhibited an optical transparency of over 57% at a wave number of 600 nm and produced bending displacement performance ranging from 29 to 946  $\mu\text{m}$  as functions of frequency and voltage. The focus variation was clearly demonstrated under actuation to study its feasibility in variable-focus lens and various opto-electro-mechanical devices. However, its transparency is low for optical application.

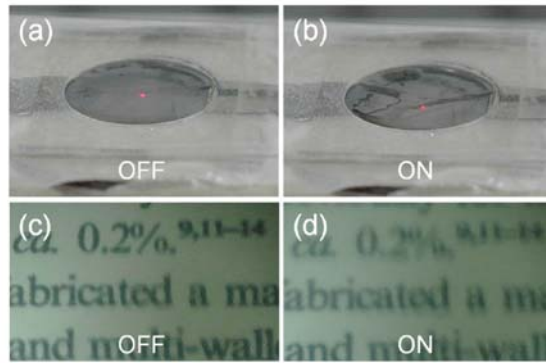


**Figure 37. (Top) FLG-driven actuator and transmitted text (bottom) with voltage “OFF” (left) and “ON” (right).[77]**

Another approach is a thin film active-lens consisting of a dielectric elastomer (DE) membrane actuator capable of dynamic vertical movement upon application of an electric field.[78] Figure 38 shows the images obtained from the lens (1 mm diameter) by applying different electric field during dynamic operation at 1 Hz. Total length of the object with four letters is 300  $\mu\text{m}$ . The active-lens is composed of a convex hemispherical poly dimethylsiloxane (PDMS) lens structure working as an aperture and a DE membrane actuator, which is a combination of a thin DE layer made with PDMS and a compliant electrode pattern using silver-nanowires. The active-lens is capable of dynamically changing the focal point of the soft aperture as high as 18.4% through its translational movement in the vertical direction responding to electrically induced bulged-up deformation of the DE membrane actuator. The responses are fast, fairly reversible, highly durable during continuous cyclic operations, and large enough to impart dynamic focus tunability for optical zoom in microscopic imaging devices with a light-weight and ultra-slim configuration.

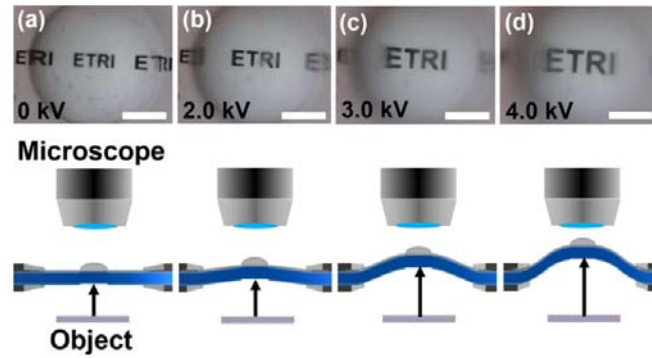


**Figure 38. Diagram of tunable lens deformation with DE membrane actuator.[78]**

However, for dielectric elastomer based tunable lens, a compliant electrode to operate the dielectric elastomer should be optically transparent and highly resistive against repetitive large deformation. Although existing stretchable, transparent conductors such as graphene, carbon nanotubes (CNTs) and metallic nanowires show fairly reliable performance, these deteriorate optical transparency of the dielectric elastomer and cannot fully ensure robustness during repetitive large deformation. As an alternative, an ionic conductor that is highly stretchable, fully transparent to light of all colors, and capable of operation at frequencies beyond 10 kHz and voltages above 10 kV shows its promising performance as a compliant electrode for VHB 4910 acrylic elastomer actuator.[79] The ionic conductor is a 100  $\mu\text{m}$  thick polyacrylamide hydrogel containing NaCl as the electrolyte and also transparent to all colors. Figure 39 shows the actuator and its strain performance with actuation voltage and frequency. The actuator is designed as a dielectric elastomer between two layers of electrolytic elastomer (Figure 39a), which contracts upon an applied bias to the electrolyte layers (Figure 39b), but maintains transparency through this process

**A** Schematic diagram of the dielectric elastomer actuator structure. It consists of an Electrode, Electrolytic elastomer, and Dielectric elastomer layers. The voltage is off.

**B** Schematic diagram illustrating the actuation mechanism. When voltage is applied, the thickness of the dielectric elastomer layer contracts (indicated by a red arrow), leading to area expansion (indicated by a red arrow).

**C** Photograph of the actuator surface showing the Harvard School of Engineering and Applied Sciences logo. The voltage is off.

**D** Photograph of the actuator surface showing the Harvard School of Engineering and Applied Sciences logo. The voltage is on, demonstrating large area strain.

**E** Plot of Area strain (%) versus Applied voltage (kV) for three samples. The data points show that area strain increases with applied voltage, reaching approximately 150% for Sample #3 at 18 kV.

**F** Plot of Area Strain (%) versus Excitation frequency (Hz) at an excitation voltage of 18 kV. The area strain decreases as the excitation frequency increases, starting from approximately 170% at 0.04 Hz and dropping to near 0% at 1024 Hz.

The scope of hydrogel applications can be enlarged from a highly transparent electrode to an electrically induced self-deformable material for tunable lens although the hydrogels have been widely used as scaffolds for tissue engineering, vehicles for drug delivery, and model extracellular matrices for biological studies. The scope of hydrogel applications, however, is often severely limited by their mechanical behavior. Most hydrogels do not exhibit high stretchability; for example, an alginate hydrogel ruptures when stretched to about 1.2 times its original length. Some synthetic elastic hydrogels have achieved stretches in the range 10–20, but these values are markedly reduced in samples containing notches. Most hydrogels are brittle, with fracture energies

The scope of hydrogel applications can be enlarged from a highly transparent electrode to an electrically induced self-deformable material for tunable lens although the hydrogels have been widely used as scaffolds for tissue engineering, vehicles for drug delivery, and model extracellular matrices for biological studies. The scope of hydrogel applications, however, is often severely limited by their mechanical behavior. Most hydrogels do not exhibit high stretchability; for example, an alginate hydrogel ruptures when stretched to about 1.2 times its original length. Some synthetic elastic hydrogels have achieved stretches in the range 10–20, but these values are markedly reduced in samples containing notches. Most hydrogels are brittle, with fracture energies

of about  $10\text{J/m}^2$ , as compared with  $1,000\text{J/m}^2$  for cartilage and  $10,000\text{J/m}^2$  for natural rubbers. Intense efforts are devoted to synthesizing hydrogels with improved mechanical properties; certain synthetic gels have reached fracture energies of  $100\text{--}1,000\text{J/m}^2$ . Electro-active hydrogels from polymers forming ionically and covalently crosslinked networks were reported.[80] Although such gels contain 90% water, they can be stretched beyond 20 times their initial length, and have fracture energies of  $9,000\text{J/m}^2$ . Even for samples containing notches, a stretch of 17 times is demonstrated. We attribute the gels' toughness to the synergy of two mechanisms: crack bridging by the network of covalent crosslinks, and hysteresis by unzipping the network of ionic crosslinks. Furthermore, the network of covalent crosslinks preserves the memory of the initial state, so that much of the large deformation is removed on unloading. The unzipped ionic crosslinks cause internal damage, which heals by re-zipping. These gels may serve as model systems to explore mechanisms of deformation and energy dissipation, and expand the scope of hydrogel applications.

### **III-2-3. Hybrid Tunable Lens**

All-solid-state tunable EAP lens is an ideal and compact tunable lens. However, in order to provide clear images of an arbitrary object located at different distance, the EAP still needs to be highly transparent and to be able to produce large deformation with low actuation voltage and fast response. To resolve this challenge, a novel design was attempted by combining optical transparency of liquids and active behavior of EAPs. A tunable lens inspired by the architecture of human eye was developed as a form of a fluid-filled elastomeric lens integrated with an annular EAP actuator working as an artificial muscle.[81] Figure 31 shows the morphological comparison between the human eye and the developed tunable lens. Upon electrical activation, the artificial muscle deforms the lens, so that a relative variation of focal length comparable to that of the human lens is demonstrated. The tunable lens provides optical performance with the benefits from compact size, low weight, fast and silent operation, shock tolerance, no overheating, low power consumption, and possibility of implementation with inexpensive and readily available elastomers.

Results show that combining bioinspired design with the unique properties of dielectric elastomers as artificial muscle transducers has the potential to open new perspectives on tunable optics.

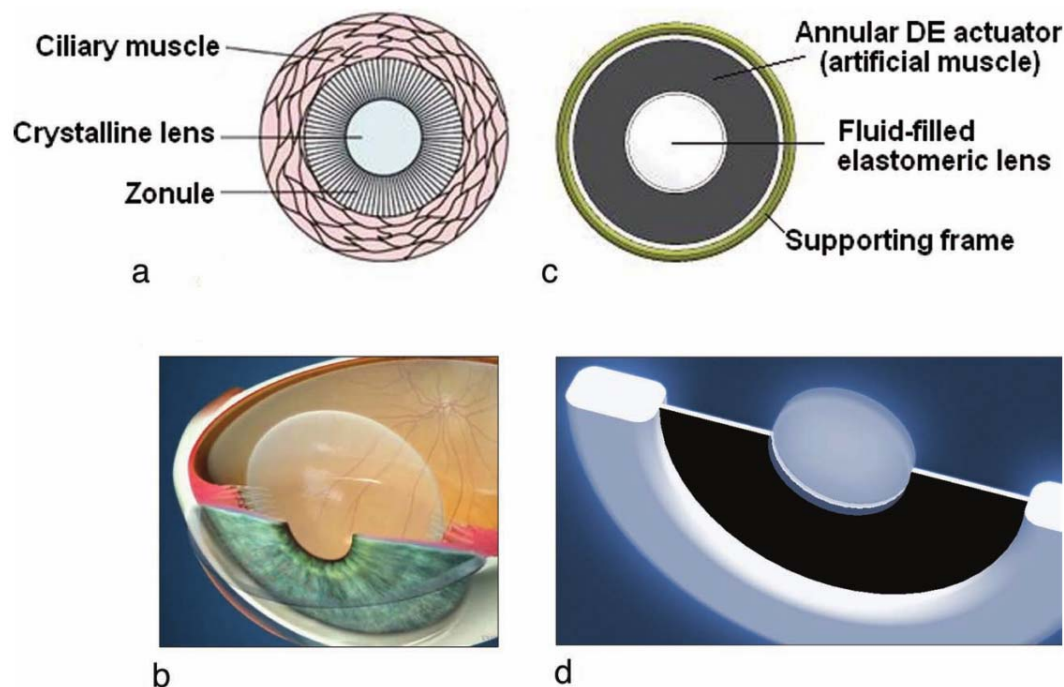


**Figure 40. Human eye (left) vs. bioinspired eye (right).** [81]

Dielectric elastomer actuators (DEA) are lightweight and flexible smart materials integrating actuation, sensing, and structural functions. To improve the simplicity and compact nature of tunable lenses, an elastomer-liquid lens system was developed, which makes use of an inline, transparent EAP actuator.[82,83] The lens requires only a minimal number of components: a frame, a passive membrane, a dielectric elastomer actuator membrane, and a clear liquid. Figure 41 shows a DEA-driven tunable lens, the world's fastest capable of holding a stable focal length, was developed.[82] By using low-loss silicone elastomers rather than acrylics (Figure 41a), a settling time shorter than  $175 \mu\text{s}$  is obtained for a 20 % change in focal length. The silicone-based lenses show a bandwidth 3 orders of magnitude higher compared to lenses of the same geometry fabricated from the acrylic elastomer. Stretchable electrodes, a carbon black and silicone composite, are precisely patterned by pad-printing and subsequently cross-linked (Figure 41b), enabling strong adhesion to the elastomer and excellent resistance to abrasion. The lenses operate for over 400 million cycles without degradation, and show no change after more than two years of storage. The lens even shows extreme resilience when stretched over a needle point (Figure 41c). This lens demonstrates the unmatched combination of strain, speed, and stability that DEAs can achieve, paving the way for complex and fast soft machines.



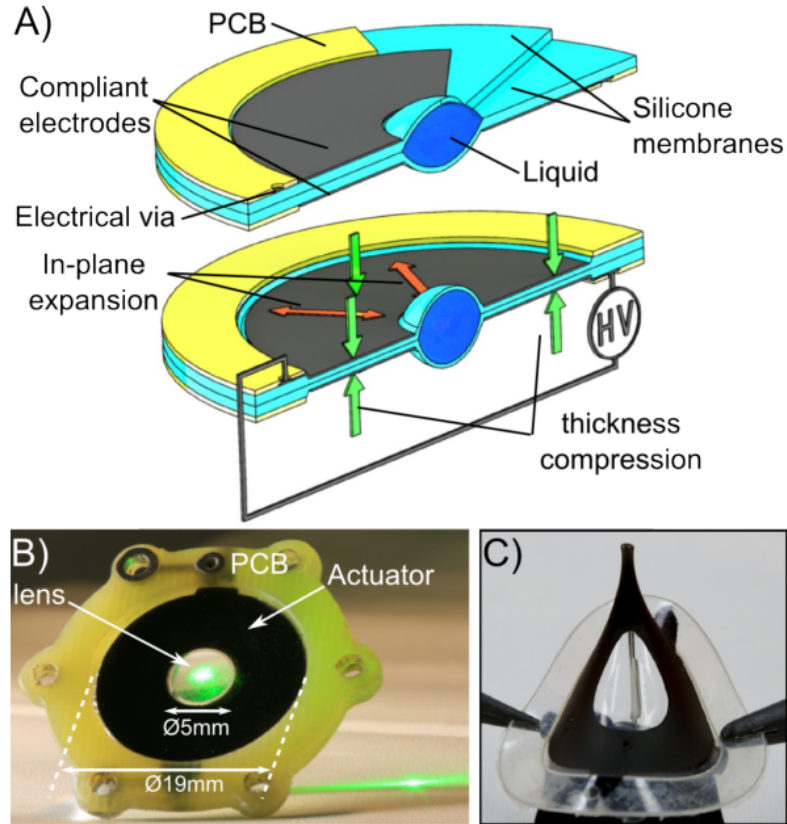


**Figure 41. DEA lens concept.**

#### **III-2-4. Acoustically Tunable Optical Arrays**

Figure 42 shows an optical lens array operating with acoustic pressure. The optical lens array whose focal length and lens pitch can be varied by acoustic radiation force was investigated.[84] It has no mechanical moving parts and a simple structure that consists of a glass plate, four ultrasound transducers, and a viscoelastic silicone gel film. A lens array can be formed by generating acoustic radiation force through flexural vibrations of the glass plate. Its focal length can be controlled by varying the voltage applied to the transducers and the lens pitch can be altered by changing the driving frequency. The lens profile is determined by the balance between the acoustic radiation force, the surface tension, and the elastic restoring force of the gel. Since the lattice modes of the glass plate have higher resonance frequencies at shorter wavelengths obtained at frequencies over 200 kHz, this technique can be used in microlens arrays in MEMS. However, using sound waves to tune this lens array forbids tuning individual lenses to specific wavelengths, and the setup is vulnerable to inadvertent noise cancellation and detuning from environmental noise.

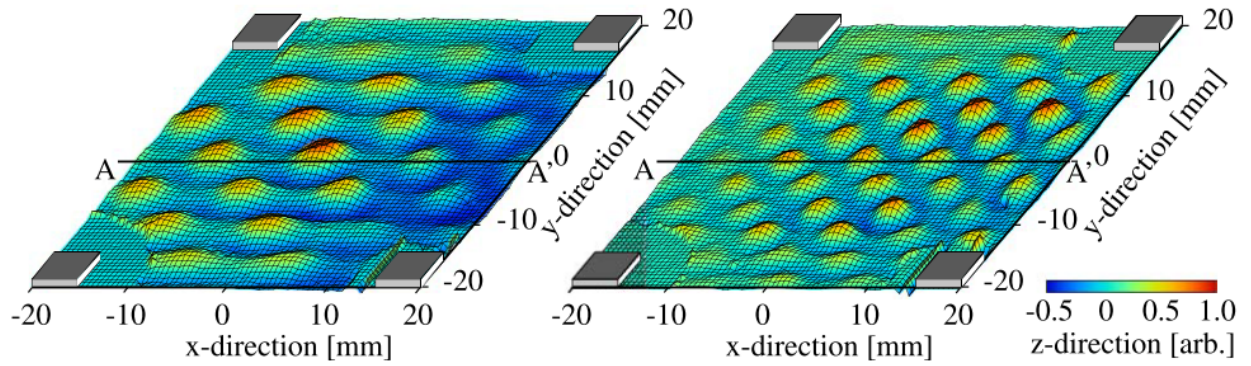


**Figure 42. Acoustically tunable silicone gel optical array at (a) 90 and (b) 170 kHz.[84]**

### III-3. Tunable Mirrors and Filters

Traditionally, telescope mirrors have taken the form of thick metal or glass disks for rigidity and precise shape. As advances in astronomy demanded larger and larger telescopes, the mirrors became thicker and ever more massive, but this trend was unsustainable. In the 1990s, developers adopted active optics for large telescopes, and the current generation uses thin, flexible mirrors that maintain their shape by a system of external actuators that push and pull on the surface. Tunable mirrors based on smart materials were developed (left side in Figure 43).[85] Imaging-quality optical mirrors have been developed by using carbon nanotubes embedded in an epoxy matrix (CNT/E). The development is notable in two ways. First, CNT/E is a known smart material capable of self-sensing and actuation, therefore opening a new path to development of light weight and ultra-compact space telescope optics and structures. Second, the starting material is a liquid, which lends itself to the fabrication of large mirrors (either segmented or monolithic) with novel support structures made possible by modern techniques such as 3D printing. A new class of lightweight mirrors with integrated supported structures, made possible by the combination of CNT/E technology, topology optimization, and 3D printing (right side in Figure 43).[86]

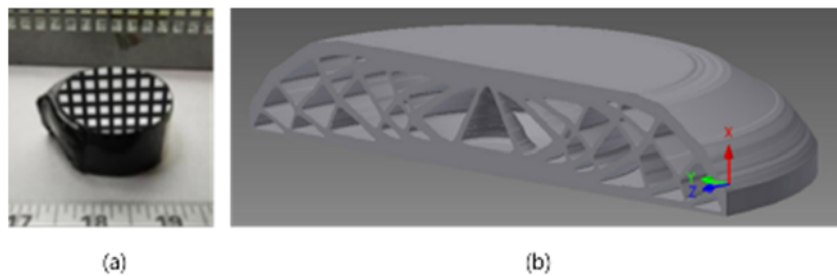


**Figure 43. (a) Image of 5 cm mirror made with CNT/E,[83] and (b) a lightweight CNT/E mirror concept.[86]**

In reverse design of lens, an electrostatic deformable mirror (EDM) was invented.[87] Figure 44 shows the configuration of the EDM operating under a voltage applied between an active mirror and a basement. The EDM is composed of a metal coated elastomeric membrane (active mirror) and a polymeric basement with electrode (ground). When an electrical voltage is applied across



the components, the active mirror deforms toward the stationary basement responding to electrostatic attraction force in an air gap. Since the differentiated gap distance can induce change in electrostatic force distribution between the active mirror and the basement, the EDMs are capable of controlling deformed geometry of the active mirror with different basement structures (concave, flat, and protrusive). Even under dynamic operations, the EDM shows fairly consistent and large deformation enough to change focal length in a wide frequency range of 1 to 175 Hz. The geometric modulation of the active mirror with dynamic focus tunability can allow the EDM to be an active mirror lens for optical zoom devices as well as an optical component controlling field of view.

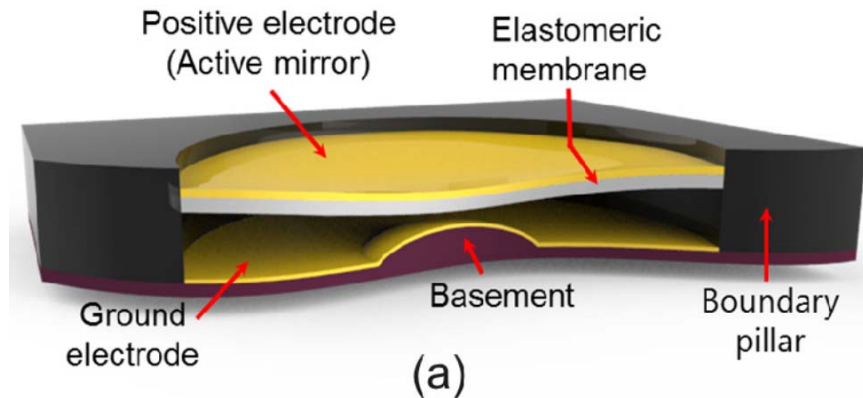


**Figure 44. An electrostatic deformable mirror.[87]**

Hydraulically-tunable hyperchromatic lenses for two-dimensional spectrally-resolved spectral imaging was developed.[88] These hyperchromatic lenses, which are composed of a positive diffractive lens and a tunable concave lens, are designed to have a large longitudinal chromatic dispersion and thus axially separate the images of different wavelengths from each other. Two-dimensional objects of different wavelengths can consequently be imaged using the tunability of the lens system. Figure 45 shows two hyperchromatic lens concepts. The hyperchromatic lenses demonstrated their spectral characteristics as well as their functionality in spectral imaging applications. As with the tunable liquid lens, this design cannot function in vacuum or space due to outgassing problems.

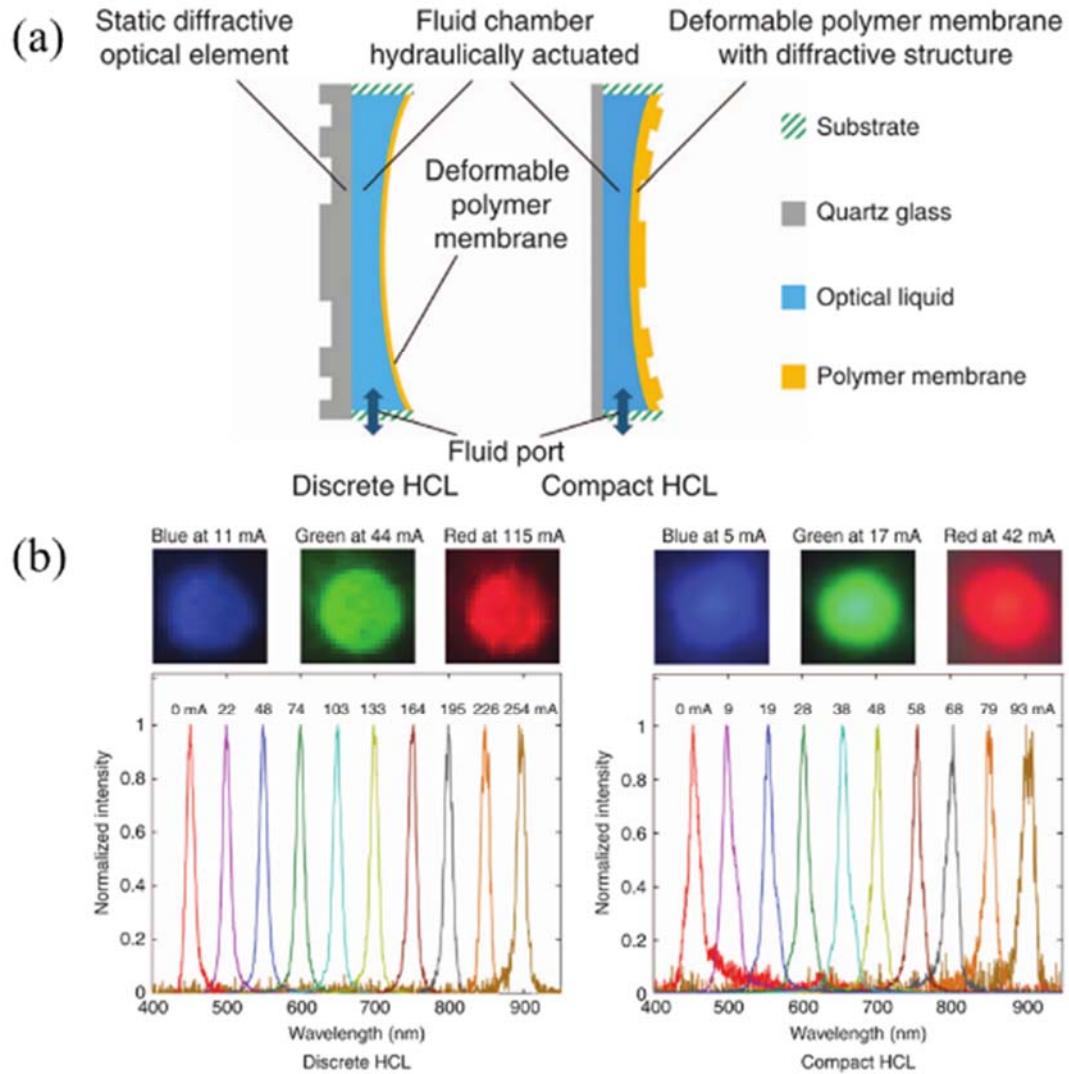


**Figure 45. (a) Hyperchromatic lens designs and (b) chromatic confocal measurement results for both designs.[88]**

A tunable micro Fresnel lens was made by a polydimethylsiloxane/carbon nanotubes (PDMS/CNTs) configuration that can change its focal length by simply stretching the substrate.[89] The Fresnel lens is formed by embedding vertically aligned CNTs bundles in a 2 mm thick PDMS layer (Figure 46). It utilizes the transparency and flexibility of the PDMS and the excellent optical absorption properties of CNTs. The lens was fabricated using a straightforward process, which requires only one lithography step. Preliminary results show that this Fresnel lens has good optical properties, and can change its focal length through simply stretching the polymer substrate.

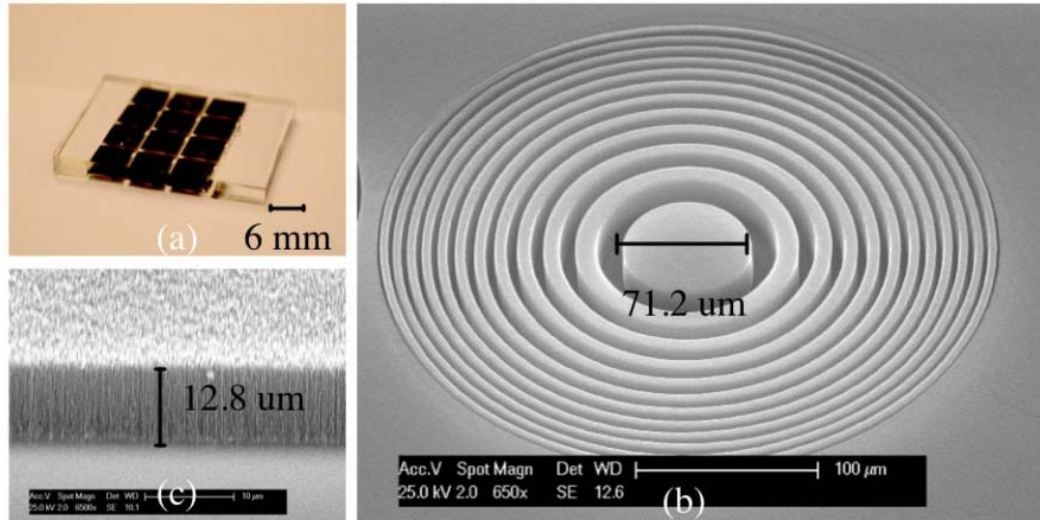


**Figure 46. (a) The fabricated device of 3×4 array of lenses. (b) Plan and (c) cross-sectional SEM images of the Fresnel lens pattern.[89]**

#### IV. Concluding Remarks

Several areas of the emerging smart optics field show many advantages over conventional optics. Various ways of changing optical behavior include refractive index modification with the Stark and Zeeman shift effects, or through tunable lenses that change shape under applied electric field. All permit one lens to do the work of many lenses, enabling many new applications and consolidating several lenses into one compact device for current applications.

Several quantum mechanical methods were discussed for modifying optical properties. The Stark effect causes a refractive index shift under an externally applied electric field according to the Kramers-Kronig relationship, while the Zeeman effect is the same concept but with an external magnetic field. Electrochromic effects involve a shift in ion distribution to produce a selective filtration of light wavelengths depending on applied bias. Birefringence effects also factor into smart optical materials, and are observed in non-cubic crystalline solids, polymers, and liquids. The splitting of incoming light into two polarizations and the responsivity of these materials to applied electric fields or mechanical stress makes for tunable optical properties and polarization. Gyrotropicity is an analogous phenomenon, using applied magnetic fields to control the polarization within a material.

Physical and mechanically responsive optics can be used to make smart optical devices and tunable lenses capable of changing several properties, including focal distance and position, reflective and refractive indices, and optical angle and intensity. Ferroelectric materials such as BaTiO<sub>3</sub> change shape from atomic rearrangement within its crystal lattice. Dopants of Eu, Sm, or Dy give BaTiO<sub>3</sub> a strong response to certain wavelengths. Amorphous films of GaScN produce an interesting shift of refractive index and extinction coefficient to higher photon energies at applied voltages of 4-5V. Much work remains to be done in this promising area of optical manipulation.

Surface plasmon polariton optics occur only in metals, transmitting light through nanometer-sized holes as incident light is converted into surface plasmons, which migrate through the holes, then emit light on the other side. A hole diameter above  $\lambda/4$  transmits a given wavelength  $\lambda$ , while

holes smaller than this threshold do not. This permits fine control over the optical properties of a fabricated array of holes. Arrays of holes, combined with an electrode for applying gate voltage, can be made into a wavelength-selective device that focuses each wavelength to a different point, and can resolve spectra without the aid of a monochromator.

Micro zone plate (MZIP) rings consist of concentric etched rings of decreasing thickness with increasing diameter to exploit the Fresnel diffraction effect. A transparent MZIP will produce different focal spots, depending on the distance from the incident light source, and when produced atop an electro-optic layer, a solid state tunable lens becomes possible, suitable for compact spectrometers. Other microfabrication applications to smart optics appear in beam scanner microchips. These force light through successive transmissions, resulting in an overall change in the incident light path after passing through the device, enabling beam deflection and redirection without mirrors.

Tunable lenses come in different forms. Dielectric liquid lenses use a pair of liquids, one with a low dielectric constant and the other with a high constant. When an electric field is applied, these droplets change shape and focal distance even on curved substrates. Other approaches include electro-active polymers (EAPs) used to mimic the human eye in a tunable polymer-based lens, deformable elastomeric microlenses that mimic anthropod eyes. All-solid-state lenses come in many types, including transparent polymer membranes around a polymer gel, bionanocomposite solid state lenses that operate under low power consumption in a responsive, biodegradable package, few-layer-graphene (FLG) electrodes on transparent elastomers, and dielectric elastomer hydrogels with very high fracture energies capable of repeated and large deformation. All of these methods respond to applied electric fields to change shape and thus focal points and distances. Hybrids of these tunable lenses were tested, where the EAP acted as the actuators to a liquid lens. As an alternative to electrically modulated lenses, silicone gel with an array of holes deforms under different frequencies of acoustical waves.

Such tunability can be applied to mirrors to reflect light rather than transmit. Carbon nanotubes in epoxy (CNT/E) are self-actuating and easy fabricated into large mirrors for more demanding space applications. Electrostatic deformable mirrors (EDMs) consist of two electrodes separated by a gap. The upper electrode is reflective and changes shape in response to applied bias on the lower electrode, changing curvature and focal properties. Hydraulic-based hyperchromatic lenses consist of fluid on a quartz substrate encased in a tunable, flexible polymer membrane, and can separate out different wavelengths from a common source. Finally, easily-fabricated MZIP rings made from PDMS and carbon nanotubes can be applied to a polymer substrate, which changes focal length when stretching the substrate.

## **Acknowledgement**

This work was supported by NASA's C&I project from 2004 to 2010, and by the National Research Foundation of Korea (NRF-2015R1A3A2066301 and NRF-2013M3C1A3059586).

## **References**

- [1] L. Premvardhan, L.A. Peteanu, P.C. Wang, A.G. MacDiarmid, Electronic properties of the

- conducting form of polyaniline from electroabsorption measurements, *Synth. Met.* 116 (2001) 157–161. doi:10.1016/S0379-6779(00)00477-X.
- [2] L.M. ROTH, B. LAX, S. ZWERDLING, THEORY OF OPTICAL MAGNETO-ABSORPTION EFFECTS IN SEMICONDUCTORS, *Phys. Rev.* 114 (1959) 90–103. [http://www.ncbi.nlm.nih.gov/entrez/query.fcgi?db=pubmed&cmd=Retrieve&dopt=AbstractPlus&list\\_uids=A1959WB76800012](http://www.ncbi.nlm.nih.gov/entrez/query.fcgi?db=pubmed&cmd=Retrieve&dopt=AbstractPlus&list_uids=A1959WB76800012).
- [3] B.O. Seraphin, N. Bottka, Franz-Keldysh effect of the refractive index in semiconductors, *Phys. Rev.* 139 (1965). doi:10.1103/PhysRev.139.A560.
- [4] D.A.B. Miller, D.S. Chemla, T.C. Damen, A.C. Gossard, W. Wiegmann, T.H. Wood, C.A. Burrus, Band-edge electroabsorption in quantum well structures: The quantum-confined stark effect, *Phys. Rev. Lett.* 53 (1984) 2173–2176. doi:10.1103/PhysRevLett.53.2173.
- [5] D.J. Griffiths, *Introduction to Quantum Mechanics*, Pearson Education, 2005. [https://books.google.com/books?id=9sqIaRGx\\_EoC](https://books.google.com/books?id=9sqIaRGx_EoC).
- [6] C.G. Granqvist, *Handbook of Inorganic Electrochromic Materials*, 1995. doi:10.1016/B978-044489930-9/50014-3.
- [7] J. Valasek, Properties of Rochelle Salt Related to the Piezo-electric Effect, *Phys. Rev.* 20 (1922) 639–664. doi:10.1103/PhysRev.20.639.
- [8] M. Melnichuk, L.T. Wood, Direct Kerr electro-optic effect in noncentrosymmetric materials, *Phys. Rev. A - At. Mol. Opt. Phys.* 82 (2010). doi:10.1103/PhysRevA.82.013821.
- [9] K. Aizu, Reversal in Optical Rotatory Power—“ Gyroelectric” Crystals and “ Hypergyroelectric” Crystals, *Phys. Rev.* 133 (1964) A1584–A1588.
- [10] G.X. Du, S. Saito, M. Takahashi, Fast magneto-optical spectrometry by spectrometer, *Rev. Sci. Instrum.* 83 (2012). doi:10.1063/1.3673638.

- [11] N. Nordman, O. Nordman, Refractive index change caused by electron irradiation in amorphous As–S and As–Se thin films coated with different metals, *J. Appl. Phys.* 90 (2001) 2206. doi:10.1063/1.1388862.
- [12] B.J. Eggleton, B. Luther-Davies, K. Richardson, Chalcogenide photonics, *Nat. Photonics.* 5 (2011) 141–148. doi:10.1038/nphoton.2011.309.
- [13] A. Spisser, R. Ledantec, C. Seassal, J.L. Leclercq, T. Benyattou, D. Rondi, R. Blondeau, G. Guillot, P. Viktorovitch, Highly selective and widely tunable 1.55- $\mu$ m InP/Air-Gap micromachined Fabry-Perot filter for optical communications, *IEEE Photonics Technol. Lett.* 10 (1998) 1259–1261. doi:10.1109/68.705609.
- [14] J.I. Steinfeld, *Molecules and Radiation: An Introduction to Modern Molecular Spectroscopy.* Second Edition, MIT Press, 1985. <https://books.google.com/books?id=D2aHDcaHccwC>.
- [15] D.C. Hutchings, M. Sheik-Bahae, D.J. Hagan, E.W. Van Stryland, Kramers-Kronig relations in nonlinear optics, *Opt. Quantum Electron.* 24 (1992) 1–30. doi:10.1007/BF01234275.
- [16] P. Grosse, V. Offermann, Analysis of reflectance data using the Kramers-Kronig Relations, *Appl. Phys. A Solids Surfaces.* 52 (1991) 138–144. doi:10.1007/BF00323731.
- [17] D. V. Lang, Deep-level transient spectroscopy: A new method to characterize traps in semiconductors, *J. Appl. Phys.* 45 (1974) 3023–3032. doi:10.1063/1.1663719.
- [18] C.W. Peterson, J. Parlett, R.S. Crandall, The physics of electrochromism: An advanced laboratory experiment, *Am. J. Phys.* 47 (1979) 772. doi:10.1119/1.11926.
- [19] P.B. Joshi, *Thin Film Variable Reflectance Materials for Solar Sail Control*, 2000.
- [20] T. Xu, E.C. Walter, A. Agrawal, C. Bohn, J. Velmurugan, W. Zhu, H.J. Lezec, A.A. Talin,



- High-contrast and fast electrochromic switching enabled by plasmonics, *Nat. Commun.* 7 (2016) 10479. doi:10.1038/ncomms10479.
- [21] P.S. Neelakanta, *Handbook of Electromagnetic Materials: Monolithic and Composite Versions and Their Applications*, CRC Press, 1995. <https://books.google.com/books?id=5w6fTx47MgsC>.
- [22] C.W. Tang, S.A. Vanslyke, Organic electroluminescent diodes, *Appl. Phys. Lett.* 51 (1987) 913–915. doi:10.1063/1.98799.
- [23] M. Abramowitz, M.W. Davidson, *Optical Birefringence*, (2012). <http://www.olympusmicro.com/primer/lightandcolor/birefringence.html> (accessed January 1, 2016).
- [24] J. Luo, S. Huang, Y.J. Cheng, T.D. Kim, Z. Shi, X.H. Zhou, A.K.Y. Jen, Phenyltetraene-based nonlinear optical chromophores with enhanced chemical stability and electrooptic activity, *Org. Lett.* 9 (2007) 4471–4474. doi:10.1021/ol701814r.
- [25] W. Wu, J. Qin, Z. Li, New design strategies for second-order nonlinear optical polymers and dendrimers, *Polymer (Guildf)*. 54 (2013) 4351–4382. doi:10.1016/j.polymer.2013.05.039.
- [26] Fujitsu, *Fundamentals of Liquid Crystal Displays – How They Work and What They Do*, (2006) 14. [http://www.fujitsu.com/downloads/MICRO/fma/pdf/LCD\\_Backgrounder.pdf](http://www.fujitsu.com/downloads/MICRO/fma/pdf/LCD_Backgrounder.pdf).
- [27] A.A. Zinchik, Application of Spatial Light Modulators for Generation of Laser Beams with a Spiral Phase Distribution, *Sci. Tech. J. Inf. Technol. Mech. Opt.* 15 (2015) 817–824. doi:10.17586/2226-1494-2015-15-5-817-824.
- [28] J. Beeckman, T. Hui, P.J.M. Vanbrabant, R. Zmijan, K. Neyts, Polarization Selective Wavelength Tunable Filter, *Mol. Cryst. Liq. Cryst.* 502 (2009) 19–28.

doi:10.1080/15421400902813626.

- [29] P.A. Franken, A.E. Hill, C.W. Peters, G. Weinreich, Generation of optical harmonics, *Phys. Rev. Lett.* 7 (1961) 118–119. doi:10.1103/PhysRevLett.7.118.
- [30] R.W. Boyd, *Nonlinear Optics*, 3rd ed., Academic Press, 2008. <https://books.google.com/books?id=uoRUi1Yb7ooC>.
- [31] R.H. Hardy, B. Nation, Acute gout and the accident and emergency department, *Arch. Emerg. Med.* 2 (1984) 89–95. <http://www.ncbi.nlm.nih.gov/pmc/articles/PMC1285204/pdf/archemed00002-0027.pdf>.
- [32] Z. Zhu, T.G. Brown, Stress-induced birefringence in microstructured optical fibers., *Opt. Lett.* 28 (2003) 2306–8. doi:10.1364/OL.28.002306.
- [33] B. Romanowicz, A. Dziewonski, *Seismology and Structure of the Earth: Treatise on Geophysics*, Elsevier Science, 2010. <https://books.google.com/books?id=5DEBDsisDEQC>.
- [34] K.J. Kingma, J.W. Downs, Crystal-structure analysis of a birefringent andradite, 74 (1989) 1307–1316.
- [35] C. Rizzo, A. Rizzo, D.M. Bishop, The Cotton-Mouton effect in gases: Experiment and theory, *Int. Rev. Phys. Chem.* 16 (1997) 81–111. doi:10.1080/014423597230316.
- [36] H. Kling, W. Hüttner, The temperature dependence of the Cotton-Mouton effect of N<sub>2</sub>, CO, N<sub>2</sub>O, CO<sub>2</sub>, OCS, and CS<sub>2</sub> in the gaseous state, *Chem. Phys.* 90 (1984) 207–214. doi:10.1016/0301-0104(84)85096-X.
- [37] C.B. Samantaray, M.L. Nanda Goswami, D. Bhattacharya, S.K. Ray, H.N. Acharya, Photoluminescence properties of Eu<sup>3+</sup>-doped barium strontium titanate (Ba, Sr) TiO<sub>3</sub> ceramics, *Mater. Lett.* 58 (2004) 2299–2301. doi:10.1016/j.matlet.2004.03.001.
- [38] A. SREENIVASULU, N. PRASAD, S. BUDDHUDU, Optical Analysis of RE 3+ (= Eu

- 3+ , Sm 3+ & Dy 3+ ): BaTiO<sub>3</sub> Ceramic Powders, Proc Indian Natn Sci Acad. 74 (2008) 1–4.
- [39] Y. Park, A. Grichener, J. Jensen, S.H. Choi, Electrical and Optical Property of Ferroelectric BaTiO<sub>3</sub> : Eu, Sci. Technol. (2005). doi:10.1117/12.590364.
- [40] M.E. Little, M.E. Kordesch, Band-gap engineering in sputter-deposited Sc<sub>x</sub>Ga<sub>1-x</sub>N, Appl. Phys. Lett. 78 (2001) 2891–2892. doi:10.1063/1.1370548.
- [41] T.W. Ebbesen, H.J. Lezec, H.F. Ghaemi, T. Thio, P. A.Wolff, T. Thio, P. A.Wolff, Extraordinary optical transmission through sub-wavelength hole arrays, Nature. 86 (1998) 1114–7. doi:10.1038/35570.
- [42] L. Martín-Moreno, F.J. García-Vidal, H.J. Lezec, K.M. Pellerin, T. Thio, J.B. Pendry, T.W. Ebbesen, Theory of extraordinary optical transmission through subwavelength hole arrays, Phys. Rev. Lett. 86 (2001) 1114–1117. doi:10.1103/PhysRevLett.86.1114.
- [43] Y. Park, J.D. Wright, J.D.L. Jensen, G.C. King, S.H. Choi, Diffraction analysis for periodic nano-scale apertures, scatterers and absorbers, Meas. Sci. Technol. 16 (2005) 2208–2212. doi:10.1088/0957-0233/16/11/011.
- [44] Y. Park, S.H. Choi, G.C. King, J.R. Elliott, Apparatus and method for creating a photonic densely-accumulated ray-point, 8,294,989, 2012.
- [45] Y. Park, L. Koch, K.D. Song, S. Park, G. King, S. Choi, Miniaturization of a Fresnel spectrometer, J. Opt. A Pure Appl. Opt. 10 (2008) 95301. doi:10.1088/1464-4258/10/9/095301.
- [46] Y. Park, S.H. Choi, Miniaturization of optical spectroscopes into Fresnel microspectrometers, J. Nanophotonics. 7 (2013) 77599. doi:10.1117/1.JNP.7.077599.
- [47] U. Lee, K.D. Song, Y. Park, V.K. Varadan, S.H. Choi, Perspective in nanoneural electronic

- implants with wireless power-feed and sensory control, *J. Nanotechnol. Eng. Med.* 1 (2010) 21007.
- [48] Y. Park, S.H. Choi, G.C. King, J.R. Elliott, Maskless Phase-Contrast Lithography with Micro Zone Plate, (2005).
- [49] Y.S. Lu, H. Tu, Y. Xu, H. Jiang, Tunable dielectric liquid lens on flexible substrate, *Appl. Phys. Lett.* 103 (2013). doi:10.1063/1.4858616.
- [50] D. Zhu, C. Li, X. Zeng, H. Jiang, Tunable-focus microlens arrays on curved surfaces, *Appl. Phys. Lett.* 96 (2010) 94–97. doi:10.1063/1.3330965.
- [51] W. Wang, J. Fang, K. Varahramyan, Compact variable-focusing microlens with integrated thermal actuator and sensor, *IEEE Photonics Technol. Lett.* 17 (2005) 2643–2645. doi:10.1109/LPT.2005.859129.
- [52] N. Chronis, G. Liu, K.-H. Jeong, L. Lee, Tunable liquid-filled microlens array integrated with microfluidic network., *Opt. Express.* 11 (2003) 2370–2378. doi:10.1364/OE.11.002370.
- [53] N. Sugiura, S. Morita, Variable-focus liquid-filled optical lens., *Appl. Opt.* 32 (1993) 4181–6. doi:10.1364/AO.32.004181.
- [54] C. Li, H. Jiang, Electrowetting-driven variable-focus microlens on flexible surfaces, *Appl. Phys. Lett.* 100 (2012). doi:10.1063/1.4726038.
- [55] X. Hu, S. Zhang, Y. Liu, C. Qu, L. Lu, X. Ma, X. Zhang, Y. Deng, Electrowetting based infrared lens using ionic liquids, *Appl. Phys. Lett.* 99 (2011) 92–95. doi:10.1063/1.3663633.
- [56] J.Y. An, J.H. Hur, S. Kim, J.H. Lee, Spherically encapsulated variable liquid lens on coplanar electrodes, *IEEE Photonics Technol. Lett.* 23 (2011) 1703–1705. doi:10.1109/LPT.2011.2167606.

- [57] C.-C. Cheng, C.A. Chang, J.A. Yeh, Variable focus dielectric liquid droplet lens., *Opt. Express*. 14 (2006) 4101–4106. doi:10.1364/OE.14.004101.
- [58] C.-C. Cheng, J. Andrew Yeh, Dielectrically actuated liquid lens, *Opt. Express*. 15 (2007) 7140. doi:10.1364/OE.15.007140.
- [59] C. V. Brown, G.G. Wells, M.I. Newton, G. McHale, Voltage-programmable liquid optical interface, *Nat. Photonics*. 3 (2009) 403–405. doi:10.1038/nphoton.2009.99.
- [60] K. Mishra, C. Murade, B. Carreel, I. Roghair, J.M. Oh, G. Manukyan, D. van den Ende, F. Mugele, Optofluidic lens with tunable focal length and asphericity, *Sci. Rep.* 4 (2014) 6378. doi:10.1038/srep06378.
- [61] N. Binh-Khiem, K. Matsumoto, I. Shimoyama, Polymer thin film deposited on liquid for varifocal encapsulated liquid lenses, *Appl. Phys. Lett.* 93 (2008). doi:10.1063/1.2988467.
- [62] Y. Bar-Cohen, Electroactive Polymer (EAP) Actuators as Artificial Muscles, Yoseph Bar-Cohen. (2004) 758. doi:10.1007/s13398-014-0173-7.2.
- [63] N. Terasawa, K. Asaka, Electrochemical and Electromechanical Properties of Activated Multi-walled Carbon Nanotube Polymer Actuator that Surpass the Performance of a Single-walled Carbon Nanotube Polymer Actuator, *Mater. Today Proc.* 3 (2016) S178–S183. doi:10.1016/j.matpr.2016.02.030.
- [64] T. Sugino, K. Kiyohara, K. Asaka, Carbon Nanotube/Ionic Liquid Composites, in: K. Asaka, H. Okuzaki (Eds.), *Soft Actuators Mater. Model. Appl. Futur. Perspect.*, Springer Japan, Tokyo, 2014: pp. 127–139. doi:10.1007/978-4-431-54767-9\_9.
- [65] Q. Shen, S. Trabia, T. Stalbaum, V. Palmre, K. Kim, I.-K. Oh, A multiple-shape memory polymer-metal composite actuator capable of programmable control, creating complex 3D motion of bending, twisting, and oscillation, *Sci. Rep.* 6 (2016) 24462.

doi:10.1038/srep24462.

- [66] S. Bhattacharya, R. Chattaraj, M. Das, A. Patra, B. Bepari, S. Bhaumik, Simultaneous parametric optimization of IPMC actuator for compliant gripper, *Int. J. Precis. Eng. Manuf.* 16 (2015) 2289–2297. doi:10.1007/s12541-015-0294-8.
- [67] S.-S. Kim, C.-D. Kee, Electro-active polymer actuator based on PVDF with bacterial cellulose nano-whiskers (BCNW) via electrospinning method, *Int. J. Precis. Eng. Manuf.* 15 (2014) 315–321. doi:10.1007/s12541-014-0340-y.
- [68] P.C. Binh, D.N.C. Nam, K.K. Ahn, Design and modeling of an innovative wave energy converter using dielectric electro-active polymers generator, *Int. J. Precis. Eng. Manuf.* 16 (2015) 1833–1843. doi:10.1007/s12541-015-0239-2.
- [69] M. Mohiuddin, H.-U. Ko, H.-C. Kim, J. Kim, S.-Y. Kim, Transparent and Flexible Haptic Actuator based on Cellulose Acetate Stacked Membranes, *Int. J. Precis. Eng. Manuf.* 16 (2015) 1479–1485. doi:10.1007/s12541-015-0196-9.
- [70] H.C. Kim, S. Mun, H.-U. Ko, L. Zhai, A. Kafy, J. Kim, Renewable smart materials, *Smart Mater. Struct.* 25 (2016) 73001. <http://stacks.iop.org/0964-1726/25/i=7/a=073001>.
- [71] S. Mun, H.-U. Ko, L. Zhai, S.-K. Min, H.-C. Kim, J. Kim, Enhanced electromechanical behavior of cellulose film by zinc oxide nanocoating and its vibration energy harvesting, *Acta Mater.* 114 (2016) 1–6. doi:10.1016/j.actamat.2016.05.021.
- [72] J.M. Choi, H.M. Son, Y.J. Lee, Biomimetic variable-focus lens system controlled by winding-type SMA actuator, *Opt. Express.* 17 (2009) 8152–8164. doi:10.1364/OE.17.008152.
- [73] Y.M. Song, Y. Xie, V. Malyarchuk, J. Xiao, I. Jung, K.J. Choi, Z. Liu, H. Park, C. Lu, R.H. Kim, R. Li, K.B. Crozier, Y. Huang, J.A. Rogers, Digital cameras with designs inspired by



- the arthropod eye, *Nature*. 497 (2013) 95–99. doi:10.1038/nature12083.
- [74] G. Beadie, M.L. Sandrock, M.J. Wiggins, R.S. Lepkowitz, J.S. Shirk, M. Ponting, Y. Yang, T. Kazmierczak, A. Hiltner, E. Baer, Tunable polymer lens, *Opt. Express*. 16 (2008) 11847. doi:10.1364/OE.16.011847.
- [75] S.-Y. Kim, M. Yeo, E.-J. Shin, W.-H. Park, J.-S. Jang, B.-U. Nam, J.W. Bae, Fabrication and evaluation of variable focus and large deformation plano-convex microlens based on non-ionic poly(vinyl chloride)/dibutyl adipate gels, *Smart Mater. Struct.* 24 (2015) 115006. <http://stacks.iop.org/0964-1726/24/i=11/a=115006>.
- [76] K.K. Sadasivuni, D. Ponnammam, H.U. Ko, L. Zhai, H.C. Kim, J. Kim, Electroactive and Optically Adaptive Bionanocomposite for Reconfigurable Microlens, *J. Phys. Chem. B*. 120 (2016) 4699–4705. doi:10.1021/acs.jpcc.6b01370.
- [77] T. Hwang, H.Y. Kwon, J.S. Oh, J.P. Hong, S.C. Hong, Y. Lee, H. Ryeol Choi, K. Jin Kim, M. Hossain Bhuiya, J. Do Nam, Transparent actuator made with few layer graphene electrode and dielectric elastomer, for variable focus lens, *Appl. Phys. Lett.* 103 (2013). doi:10.1063/1.4812982.
- [78] S. Yun, S. Park, B. Park, S. Nam, S.K. Park, K.U. Kyung, A thin film active-lens with translational control for dynamically programmable optical zoom, *Appl. Phys. Lett.* 107 (2015). doi:10.1063/1.4929716.
- [79] C. Keplinger, J.-Y.J.-Y. Sun, C.C. Foo, P. Rothemund, G.M. Whitesides, Z. Suo, Stretchable, Transparent, Ionic Conductors, *Science* (80-. ). 341 (2013) 984–987. doi:10.1126/science.1240228.
- [80] J.-Y. Sun, X. Zhao, W.R.K. Illeperuma, O. Chaudhuri, K.H. Oh, D.J. Mooney, J.J. Vlassak, Z. Suo, Highly stretchable and tough hydrogels, *Nature*. 489 (2012) 133–136.

doi:10.1038/nature11409.

- [81] F. Carpi, G. Frediani, S. Turco, D. De Rossi, Bioinspired Tunable Lens with Muscle-Like Electroactive Elastomers, *Adv. Funct. Mater.* 21 (2011) 4152–4158. doi:10.1002/adfm.201101253.
- [82] L. Maffli, S. Rosset, M. Ghilardi, F. Carpi, H. Shea, Ultrafast all-polymer electrically tunable silicone lenses, *Adv. Funct. Mater.* 25 (2015) 1656–1665. doi:10.1002/adfm.201403942.
- [83] S. Shian, R.M. Diebold, D.R. Clarke, Tunable lenses using transparent dielectric elastomer actuators., *Opt. Express.* 21 (2013) 8669–76. doi:10.1364/OE.21.008669.
- [84] D. Koyama, M. Hatanaka, K. Nakamura, M. Matsukawa, Ultrasonic optical lens array with variable focal length and pitch., *Opt. Lett.* 37 (2012) 5256–8. doi:10.1364/OL.37.005256.
- [85] P.C. Chen, D. Rabin, Carbon nanotube optical mirrors, *J. Astron. Telesc. Instruments, Syst.* 1 (2014) 14005. doi:10.1117/1.JATIS.1.1.014005.
- [86] P.C. Chen, D. Rabin, Using carbon nanotubes to make smart telescope mirrors, (n.d.) 10–12.
- [87] S. Nam, S. Park, S. Yun, B. Park, S.K. Park, K.-U. Kyung, Structure modulated electrostatic deformable mirror for focus and geometry control, *Opt. Express.* 24 (2016) 55–66. doi:10.1364/OE.24.000055.
- [88] P.-H. Cu-Nguyen, A. Grewe, P. Feßer, A. Seifert, S. Sinzinger, H. Zappe, An imaging spectrometer employing tunable hyperchromatic microlenses, *Light Sci. Appl.* 5 (2015) e16058. doi:10.1038/lsa.2016.58.
- [89] X. Li, L. Wei, S. Vollebregt, R. Poelma, Y. Shen, J. Wei, P. Urbach, P.M. Sarro, G.Q. Zhang, Tunable binary Fresnel lens based on stretchable PDMS/CNT composite, in: 2015

Transducers - 2015 18th Int. Conf. Solid-State Sensors, Actuators Microsystems, 2015: pp.  
2041–2044. doi:10.1109/TRANSDUCERS.2015.7181357.